Characterization of deep weathering and nanoporosity development in shale – a neutron study

Lixin Jin[1]*, Gernot Rother[2], David R. Cole[2], David Mildner[3], Susan L. Brantley[1]

1. Center for Environmental Kinetics Analysis, Earth and Environmental Systems Institute, Pennsylvania State University, State College, PA 16803, USA
2. Chemical Sciences Division, Oak Ridge National Laboratory, Oak Ridge, TN 37831, USA
3. NIST Center for Neutron Research, National Institute of Standards and Technology, Gaithersburg, MD 20899, USA

* Corresponding author: luj10@psu.edu; 814-865-9384; 503 Deike Building, Penn State University, State College, PA 16803.

Abstract: The bedrock - regolith interface is characterized by critical changes in porosity, surface area, chemistry, and mineralogy. Here, we use a combination of small-angle and ultra small-angle neutron scattering (SANS/USANS), mineralogical, and geochemical observations to characterize the evolution of nanoscale features formed by weathering of the Rose Hill shale chips from within the Susquehanna/Shale Hills Observatory (SSHO). The SANS/USANS techniques, here referred to as neutron scattering (NS), can characterize connected and unconnected pores or fractures ranging from about 3 nm to several μm in dimension that develop as bedrock transforms into regolith. The primary pores interrogated by NS in unweathered Rose Hill bedrock are isolated, intraparticle pores that comprise ~5-6% of the total rock volume. As the bedrock fragments and alters, secondary pores grow. Porosity of carbonate-poor shale chips is relatively constant above the depth marked by dissolution of carbonate around 22 m but increases in the zone of feldspar weathering that begins at 6 m depth. In that upper zone, physical processes related to peri-glacial conditions at 15 ka have also increased the porosity. The regolith, defined as the zone that is accessible by hand augering, is generally 20 to 300 cm in depth in SSHO. Centimeters below the bedrock-regolith interface, chlorite and illite begin to dissolve significantly, leading to increased porosity and surface area. As clay dissolution proceeds in rock chips throughout the regolith zone, intraparticle pores progressively connect to form large interparticle pores, changing the mineral-pore interface from a mass fractal to a surface fractal. NS documents that the pore geometry is anisotropic at depth but becomes isotropic with intense weathering.

As clay minerals become more depleted, quartz surfaces are exposed, causing the total mineral-pore interfacial area eventually to decrease and become smoother. Smoothening of weathering surfaces could be also consistent with reactions occurring close to equilibrium, as expected when transport limits chemical weathering. In the most weathered rock chips, kaolinite and Fe oxyhydroxides have precipitated, possibly blocking some of the previously connected porosity. All the NS and geochemical observations agree with a conceptual model where the conversion of bedrock to regolith at SSHO is largely due to mineral dissolution reactions and the advance is rate-limited by the rate of diffusion of reactants into the rock. To our knowledge this is the first NS study to investigate the growth of nanopore features during rock weathering from depths of tens of meters to the Earth's surface, providing novel and important information about the mechanics of weathering.

Key Words: SANS/USANS, regolith, porosity, fractal dimension, clay minerals, surface area

1. INTRODUCTION:

Regolith formation is controlled by the coupled physical, chemical and biological processes that comprise weathering (e.g., Anderson, 2005; Dietrich and Perron, 2005; Schaetzl and Anderson, 2005; Brantley et al., 2006; Fletcher et al., 2006; Anderson et al., 2007; Yoo et al., 2009). Without these reactions, life on the continents would be limited by the lack of surface area available for nutrient and energy processing (Brantley et al., 2006; Anderson et al., 2007; Graham et al., 2010). Regolith development starts when water enters the bedrock through fractures, eventually creating new surface area (Molnar et al., 2004; Fletcher et al., 2006). Fractures allow reactive gases, water, and biota to penetrate the bedrock and promote biogeochemical weathering reactions. As mineral dissolution and precipitation progress, porosity increases making bedrock more vulnerable to further dissolution and disaggregation. The transition from bedrock to regolith is thus comprised of an upward overall increase in physical surface area, porosity and chemical alteration. Eventually, at the surface, regolith becomes so disaggregated and biologically impacted that it is easily mobilized: this uppermost layer is referred to here as the mobile soil.

Despite the importance of understanding the processes by which bedrock disaggregates and water-induced chemical and biogeochemical reactions turn bedrock into regolith, little is known about the initiation and development of porosity during incipient weathering of bedrock (Merino et al., 1993; Oguchi , 2004; Fletcher et al., 2006; Green et al., 2006; Brantley and White, 2009; Navarre-Sitchler et al., 2009; Rossi and Graham et al., 2010; Ma et al., 2010). One way to study the advance rate of weathering into bedrock is to analyze weathering rind development on clasts. In one well-studied rind system, Fe oxidation appears as the first weathering reaction within basalt clasts in alluvial terraces of Costa Rica (Sak et al., 2004; Navarre-Sitchler et al., 2009). This reaction is followed by dissolution of plagioclase that opens up porosity.

These same reactions, Fe oxidation followed by plagioclase dissolution, are shown to be important in controlling the advance of the bedrock/saprolite interface in quartz diorite of Puerto Rico (Fletcher et al., 2006). In that system, water enters the rock through relatively vertical joints and fractures. Unlike the basalt clasts, however, concentric fractures form in both vertical and horizontal 30-cm thick sets that disaggregate the bedrock into coherent onionskin-like rindlets. These rindlets exhibit decreasing bulk density and an increase in microcrack density with increasing distance from the unaltered corestone (Buss et al., 2008). Petrographic examination indicates that iron oxidation in biotite, presumably accompanying its transformation to a K-deficient and Fe(III)-enriched ‘altered biotite’ phase, occurs within the previously unaltered rock. This reaction is inferred to be accompanied by a volume increase that induces the spheroidal fracturing (Fletcher et al., 2006; Royne et al., 2008; Graham et al., 2010). However, this complex

interplay of fracturing and chemical reaction is also accompanied by biological activity: a microbial ecosystem is growing at the bedrock-saprolite interface that may also be involved in Fe oxidation at the bedrock-saprolite interface (Buss et al., 2005). Furthermore, mycorrhizal fungi exude organic acids to form cylindrical pores of diameter 3-6 μm in rocks, presumably contributing to transformation of bedrock to regolith in some localities (Jongmans et al., 1997; van Breemen, 2000).

This production of regolith from bedrock at depth is paralleled at the surface by production of a mobile soil layer within regolith. Researchers have suggested that the soil production rate may either exhibit a hump function (increase and then decrease with soil depth) or simply decrease exponentially with increasing soil thickness (e.g., Cox, 1980; Heimsath et al., 1997; Minasny and McBratney, 1999; Ma et al., 2010). The decline in the rate of mobile soil production with increasing soil depth could result strictly from chemical effects related to the decrease in reactivity of infiltrating fluids as these fluids move closer towards chemical saturation with depth (Jin et al., 2008; White et al., 2009). Alternately, the soil production function could be dictated largely by physical processes. For example, fracturing by frost wedging occurs in polar and alpine regions when water trapped in cracks expands upon freezing (Murton et al., 2006; Matsuoka and Murton, 2008). Shear deformation and freeze-thaw cycling has been hypothesized to decrease with depth as the range of soil temperatures decreases with depth. Insolation may also induce fractures in densities that decrease with depth when the stress from thermal gradients exceeds the tension limit in the upper layers of arid and semi-arid regions (McFadden et al., 2005). However, biota are also implicated in the production of mobile soil, such as animal burrowing, tree throw and root growth, although the extent to which biota modulate sediment transport is largely unknown (e.g., Roering et al., 2001; Gabet et al., 2003).

Neutron Scattering:

Several methods have been employed to study the pores and interfacial features of sedimentary rocks (Avnir et al., 1984; Wong et al., 1986; Krohn, 1988; Pernyeszi and Dekany, 1993; Smucker et al., 2007). The small-angle neutron scattering (SANS) and ultra small-angle neutron scattering (USANS) techniques, here referred to as neutron scattering (NS), are suitable for investigation of features ranging from about 3 nm to 10 μm in size. Extensive reviews are available for the applications of NS techniques in rock studies (e.g., Radlinski, 2006; Agamalian, 2009). Early studies have focused on how surface area, porosity, and pore size distribution in sedimentary rocks relate to production and transport of natural gases and oil (e.g., Radlinski et al.,

1999, 2004). In recent years, NS techniques have become powerful tools in other fields of geology (e.g., Lucido et al., 1988; Kahle et al., 2004; Anovitz et al., 2009; Cole et al., 2009).

Neutrons easily penetrate bulk materials, probing the interior structure by scattering off the interfaces and objects, when the phases differ in neutron coherent scattering length density (SLD). Rocks can commonly be modeled as random two-phase systems comprised of pores and mineral matrix, which have distinct and different SLDs (e.g., Radlinski, 2006). Furthermore, hydrogen isotopes have contrasting neutron coherent scattering lengths; mixing different proportions of H and D can produce water of different SLD, a property that can be effectively used to probe accessible or connected versus total porosities. Specifically, the amount of unconnected pores can be measured by matching the SLD of a D_2O/H_2O mixture to that of the mineral matrix, so that all filled (connected) pores disappear from the scattering pattern.

In this study, we coupled previously published (Jin et al., 2010) and newly collected chemical, mineralogical, and physical characterization data with neutron scattering observations to investigate weathering profiles developed on grey shale. We hypothesized that chemical reactions dominate in initiating the bedrock alteration and porosity development. We addressed the following questions: 1) How does porosity evolve as a function of depth in the shale? 2) How are changes in chemistry and porosity interrelated? 3) What is the mineral-water interfacial area in the unaltered rock and how does it change with reaction progress? 4) Can the rock-pore interface be described as a fractal system? 5) What proportions of pores are connected and thus accessible for water-rock interaction? Since the focus of this study, the Rose Hill Formation, is a relatively oxidized end-member shale composition and generally low in porosity, diffusion may be the dominant mode of transport for reactants and products to and from the weathering interface in the intact rock. Under conditions where diffusion dominates transport, small changes in porosity will have a major influence on reactive surface areas and thus the chemical reaction kinetics. In this communication, we report analyses of rock fragment chips in samples derived from depths ranging from 10 cm (in regolith) to 22 m (in bedrock).

Geological Setting:

Our study site is the Susquehanna/Shale Hills Observatory (SSHO), a Critical Zone Observatory located in central Pennsylvania (Fig. 1A). The SSHO is underlain by the Rose Hill Formation of the Clinton Group; olive-pink, grayish-buff shales with a few interbedded limestones (Folk, 1960; Lynch and Corbett, 1985). The Rose Hill Formation is locally characterized by fracture cleavage that has produced pencil-like fragments up to 30 cm long (Flueckinger, 1969). The geologic structure in the region is characterized by tight plunging folds

in Silurian-aged strata where strike and dip measured on a bedrock outcrop along the valley floor in the catchment are N54^{o}E and 76^{o}NW, respectively. However, borehole televiewer studies near the entrance of the catchment indicate more gentle dips of approximately 25^{o}, consistent with folding and faulting underlying the small watershed

This V-shaped SSHO catchment has south-facing and north-facing slopes averaging 23 ^{o} and 28^{o}, respectively. The erosion rate averaged over the entire catchment is estimated to be 15 m/million years based on meteoric cosmogenic nuclide ^{10}Be dating of sediments while the regolith production rates (= weathering advance rates) decrease with increasing soil thickness from 10 to 40 m/million years based on U-series isotope analysis of soils along the north-facing slope (Jin et al., 2010; Ma et al., 2010). Chemical weathering at SSHO was investigated by comparing bulk chemistry and mineralogy in profiles drilled into Rose Hill shale bedrock (recovered from a 25-m drill core) and augered into soils (Jin et al., 2010).

Here, we describe the progression from relatively unfractured and chemically unaltered parent rock ("bedrock") to intact and in-place rock that is somewhat fractured and altered ("saprock") to rock which is disaggregated and highly altered ("regolith"). In addition, on sloped terrain, we use the term "soil" to refer to the layer of regolith that moves downslope. Operationally in this location using these definitions, bedrock and saprock must be drilled with a diamond bit or something similar using gasoline or electrical power. In contrast, regolith and soil can be augered by hand. The deepest boundary of saprock is defined here as the interface where elemental or mineralogical analysis delineates the occurrence of the first chemical weathering reaction; the deepest boundary of soil is defined by textural observations that document lateral grain movement. Regolith thickness varies from 30 cm at the northern ridgetop where a deep core was drilled, to more than 3 m in some locations at the valley floor (Lin and Zhou, 2007; Jin et al., 2010).

Variations in Rose Hill shale composition and the structural complexities make it difficult to distinguish local heterogeneities in shale layers from reaction zones due to weathering. Nonetheless, two weathering fronts have been hypothesized from observations of the core drilled at the northern ridge; the deepest inferred reactive interface (or "reaction front") involves ankeritic carbonate dissolution at about 22 m below ground surface at the ridge. The next shallower reaction front is defined by plagioclase feldspar dissolution which begins at about 5 m below ground surface at the ridge top (Fig. 1B; Jin et al., 2010). At this latter depth, a decrease in the bulk density of rock chips recovered from drilling was also observed. In the drilled cores where ankerite is absent, X-ray diffraction (XRD) data and scanning electron microscope (SEM) images show that shale is comprised of illite (54 wt%), quartz (34 wt%) and "chlorite" (9 wt%),

with a few percent feldspar and Fe-oxides (Jin et al., 2010). Here, "chlorite" indicates a 'vermiculited' chlorite, with XRD peaks at values of 2Θ equal to about 14°.

In contrast to carbonate and feldspar dissolution, clay dissolution has only been documented within regolith (Fig. 1B). The dominant weathering reactions in the regolith were determined to be the dissolution of "chlorite" and illite accompanied by precipitation of kaolinite and Fe-oxyhydroxide, with vermiculite and hydroxy-interlayed vermiculite as intermediate phases. The abundance of the secondary phases kaolinite and Fe-oxyhydroxide generally increased upward in soils. These mineral transformations in the regolith are consistent with the observed losses of major cations (Al, Fe, Mg, K, Si) and are accompanied by decreases in bulk density (Jin et al., 2010).

2. METHODS

Neutron scattering experiments were conducted on shale chips that were recovered from two ridgetop regolith profiles and from one 25-m core drilled at the northern ridgetop (Fig. 1A; Table 1). Five samples were taken from the drill core (DC1) of Rose Hill shale (DC40, DC160, DC540, DC620, and DC1990, where the number refers to depth below land surface in cm). Of these five, DC40 and DC160 lie above the weathering zone of plagioclase dissolution whereas DC540, DC620 and DC1990 lie beneath that zone but above the zone of carbonate dissolution.

Seven chips from two regolith profiles (SSRT5, SSRT15, SSRT22, SSRT27; and SPRT5, SPRT15, SPRT25; numbers refer to depth below land surface in cm) represent shale rock fragments in the zone where clays are weathering. These two profiles were sampled by hand augering to refusal at two ridge top positions in the southern side of the Shale Hills catchment, one at the top of a planar hillslope (SPRT, initials refer to south planar ridge top) and the other at the top of a hillslope characterized by a swale (SSRT, initials refer to south swale ridge top). At these ridge top sites, soils are developed in-situ from shale with insignificant addition of new material from upslope (along the ridge). Furthermore, at these sites water flows mostly vertically; therefore, shallow soils have experienced longer and more intense chemical weathering than the deeper soils (Fig. 1B). The two ridge profiles examined in this study were less than 20 m apart and exhibited similar physical properties and soil thickness (Fig. 1A).

To calculate the SLD of the mineral matrix, chemical composition and grain density were measured. Grain densities of shale chips from drilled bedrock and from soils were previously determined by pycnometer (~ 2.62 g/cm^3) (Jin et al., 2010). Chemistries of the drill core and regolith chips, including those used for this study were also previously reported (Jin et al., 2010).

Total Fe content of soils was determined by lithium metaborate fusion and inductively coupled plasma atomic emission spectroscopy (ICP-AES) at the Material Characterization Laboratory of Pennsylvania State University, and the ferrous Fe was titrated following Goldich (1984). A US Geological Survey reference material (SCo-1, Cody Shale) was run as a standard. Repetitive analyses show that ferrous Fe titration on shales is accurate to within ±3%. The carbon content was estimated from published loss on ignition data, assuming CH_2O stoichiometry (Stevenson and Cole, 1999; Tan, 2003; Jin et al., 2010).

Because H has a significantly different coherent scattering amplitude from other elements, H content in shale chips was quantified using the NG7 Prompt Gamma Activation Analysis (PGAA) spectrometer at the National Institute of Standards and Technology (NIST) Center for Neutron Research (NCNR) (Failey et al., 1979). The formula of an 'artificial' compound was then created with the stoichiometry determined from the chemistry of major elements for all samples. The SLD of the mineral matrix in each sample was then calculated from the chemical sum formula and grain density using the NIST SLD calculator (http://www.ncnr.nist.gov/resources/sldcalc.html).

The chips, recovered from drilled or augered cores, were slightly elongated with dimensions on the order of about 10 cm x 5 cm on the bedding plane, and 5 cm in thickness. To prepare samples for scattering, the chips were dried at room temperature and cut parallel to the bedding. Thin sections were commercially prepared and put on quartz slides, because standard boron-containing glass slides absorb neutrons. The samples were uniformly cut to be 150 μm thick to prevent multiple scattering (Anovitz et al., 2009). Thus, the data we collected represents the single-scattering cross section.

The principles of neutron scattering are discussed in the literature (e.g., Guinier and Forner, 1955) and are only briefly summarized here. A neutron beam propagates into a sample, where it is elastically scattered. Detectors measure the scattering intensity I(Q) in units of cm^{-1}, as a function of the scattering angle, which is defined as the deviation from the incident beam. The scattering vector Q in units of $Å^{-1}$, is related to scattering angle 2θ by $Q = (4\pi/\lambda) \sin\theta$, where λ is the wavelength of the neutron beam. Thus, the size range of features accessible with SANS and USANS is dependent on the neutron wavelength λ and the range in scattering angle 2θ. 2θ generally ranges from 4′ to 10° for SANS and 6¨ to 5′ for USANS.

In rocks, coherent scattering within a given Q-range is dominantly contributed by objects whose size or spacing is on the order of $2\pi/Q$ (Bragg, 1913). The contribution from hydrocarbons to the overall scattering is assumed to be minimal, because scattering density is almost zero for hydrocarbon and the contrast between mineral-hydrocarbon is approximately the same as that of

mineral-pore (Hall et al., 1983). Therefore, most scattering in rocks is due to mineral-pore interfaces, regardless of whether the pores are filled with hydrocarbons or air.

Neutron scattering experiments were carried out at NCNR, and instrumentation details are given on the NCNR website (http://www.ncnr.nist.gov/instruments/). Apertures of different sizes in a Cd mask were used to define the illuminated sample area. Measurements were made on the NG7 30-m SANS beamline with an incident neutron wavelength of 8.09 Å and sample-detector distances of 1m, 4m and15.3m. By using confocal MgF_2 lenses at the long sample-detector distance and a horizontal detector offset at the short sample-detector distance, these positions covered a large Q-range from 0.0008 $Å^{-1}$ to 0.7 $Å^{-1}$ (Glinka et al., 1998). This range corresponds to length scales between 10 Å and 0.8 μm. Two-dimensional scattering intensity data were collected for each sample and corrected for empty beam scattering, background counts (using a blocked beam and empty quartz slide), and detector uniformity. The scattering intensity data were reduced to an absolute scale by normalization to the flux of the empty neutron beam. The two-dimensional SANS data were also circularly averaged to produce one-dimensional intensity profiles.

The BT5 USANS covers a Q-range from 0.00003 $Å^{-1}$ to ~ 0.002 $Å^{-1}$, corresponding to scattering due to features of length or spacing between 0.06 and 20 μm (Barker et al., 2005). A fixed Cd mask in front of the sample ensured that the same sample areas were measured on SANS and USANS. The duration of NS measurement per sample was based on the count rates of the samples. Scattering data were corrected for empty cell scattering, neutron background, and normalized to the sample transmission. SANS and USANS raw data were reduced and normalized (including the deconvolution of the USANS data by desmearing for slit-height corrections) using NCNR data reduction software (Kline, 2006) and IGOR Pro.

To determine the fraction of pores (or cracks) that are connected, we carried out SANS/USANS measurements on one set of samples that was measured first dry, and then subsequently saturated with a D_2O-H_2O mixture of identical SLD to that of the mineral matrix (mass ratio of H_2O:D_2O = 64%:36%). The difference observed in scattering intensities between the dry and wet samples is caused by the disappearance of NS from connected pores. To accomplish this, a select number of representative thin sections used for previous porosity measurements were soaked in acetone for two days, which yielded samples completely detached from the quartz slides. Each sample was then put on top of a quartz slide, which was encased by gluing another quartz slide with a rubber gasket (1.66 mm thick) in between. The specially mixed D_2O - H_2O solution was then injected into the quartz slide 'sandwich' through the gasket with a syringe and a needle. Samples were soaked in the D_2O-H_2O solution for one week to ensure

complete pore filling of the mixture, and measured on SANS/USANS under the same conditions as the dry samples.

Scanning electron microscopy (SEM) and transmission electron microscopy (TEM) were used to image shales that have been weathered to different degrees, to check the interfacial features at different spatial scales. The samples used for SEM were the same thin sections used for SANS/USANS experiments. Images were taken for SSRT5 and SSRT27 on an environmental SEM (FEI Quanta 200) in the Materials Characterization Laboratory at the Pennsylvania State University. These samples were also analyzed under TEM. To make the TEM sections, a thin slice was cut from a bulk piece of shale, glued to a 3mm copper ring, then dimpled and argon-ion milled using a Gatan Precision Ion Polishing system at 5kV and 7° incidence angle, until perforation. The electron transparent foil was coated with about 2nm of carbon by evaporation, prior to examination in a Hitachi HF-3300 cold field-emission TEM at the Oak Ridge National Laboratory, operated at 300kV. The thin carbon film stabilized the foil against charging from the incident electron beam. Energy dispersive x-ray spectra were acquired on the TEM using a ThermoNoran EDS system.

3. RESULTS

Scattering curves:

The raw scattering intensities for all samples are reported in Supplement Table 1. USANS and SANS data overlap for a couple of data points in each sample and are well connected when plotted as I(Q) versus Q (e.g., DC160 in Fig. 2). Such overlap is indicative of high quality data for both instruments. In the high-Q region of the SANS data, scattering intensities level off and remain constant at the incoherent scattering background level.

Overall, the absolute scattering intensities for shale chips from the shallow soils are greater than those for samples from deeper soils and from bedrock, especially at ultra small-angles (Fig. 3): scattering intensity increases as weathering progresses. Furthermore, the samples from relatively shallow depths of the drilled core (DC40, DC160) scattered neutrons more intensively than the deeper samples (DC540, DC620, DC1990) over the entire Q-range (Fig. 3A). In the low-Q range, shale chips from shallow soil depths also scattered neutrons more strongly than those from deeper depths (Figs. 3B and 3C). However, no such trend was observed in the high-Q range.

For all samples, the scattering intensity varies with the scattering vector according to a power law relationship (straight lines on log-log plots) after correcting the background at high Q for the incoherent scattering (resulting mostly from hydrogen in the sample) (Fig. 3):

$$I(Q) = A \times Q^{-n} + B \qquad (1)$$

Here, the slope gives the Porod exponent *n*, *A* is a proportionality constant, and *B* represents the contribution from incoherent scattering. The normalized scattering curves from the individual samples were fit to this equation, yielding slopes (*n* values) provided in Table 1 and plotted in Figure 4A. The deepest samples from the two soil profiles and from the bedrock have slopes between 3 and 2. In contrast, the chips from shallow soils have slopes between 4 (indicating a smooth pore surface) and 3.

Nano-porosity:

Scattering intensities depend on the density of the interfacial features within the thin sections. We interpret the scattering data quantitatively and calculate nano-porosity (P) by using a random two-phase approximation (mineral matrix-pore space) (Porod, 1952):

$$\int_0^{Q_{\max}} I(Q) Q^2 \, dQ = Z = 2\pi^2 \times (SLD)^2 \times P \times (1 - P) \qquad (2)$$

Here, Z is the scattering invariant, calculated by integrating the term Q^2 I(Q) over the measured Q-range; SLD (the scattering contrast) is the scattering length density of the mineral matrix (= 0 for empty pores). Porosity measured by neutron scattering using equation (2) has been shown to be in general agreement with that measured by gas adsorption methods (Hall et al., 1983), especially when measured over a wide Q-range, as in this study. The SLD values and the corresponding porosities are reported in Table 1.

The shale samples from beneath the bedrock-regolith interface comprise two distinct groups: a shallow group (< 5 m) with porosity as high as 9.3%, and a deeper group (> 5 m) with an average porosity ~5-6% (Fig. 4B). Interestingly, this increase in porosity continues in chips from above the bedrock-regolith interface upwards to the ground surface in the soil profiles: porosity equals about 8% at 30 cm and 14-16% at 10 cm.

The software program PRINSAS has been developed to analyze scattering data on sedimentary rock systems (Hinde, 2004; Radlinski, 2006). Scattering data were analyzed in PRINSAS to derive Porod exponent and porosity values that were compared to our calculations (Table 1). The Porod exponents from the calculations are in good agreement (± 2%) with our calculation. However, the porosity values obtained from PRINSAS were systematically lower

than our values. This may be due to a larger value of the incoherent scattering background assumed in PRINSAS than what was used by our calculation.

Surface area:

PRINSAS was used to calculate specific surface area (SSA). SSA varied significantly with depth (Fig. 4C). The least weathered shale chips (DC540, DC620, DC1990) have low SSA between 30-60 m^2/g, well within the range of surface areas determined by gas absorption methods for typical shales from depths of 500-3500 m (Radlinski et al., 1999). As weathering progresses, SSA of the shale chips increases gradually to 100 m^2/g (DC40 and DC160) and eventually reaches 300 m^2/g at 30 cm below the land surface (SSRT27, SPRT25). SSA of the chips then decreases back to 40 m^2/g at 10 cm and 20 cm (SSRT5 and SPRT5), although the porosity continues to increase in these samples. The specific surface area of typical soils, measured on another SSHO soil core by nitrogen adsorption and the Brunauer-Emmett-Teller (BET) isotherm (Gregg and Sing, 1967), equals 22-30 m^2/g (Jin et al., 2010).

Anisotropy:

Although the thin sections were cut parallel to bedding, the shales exhibited elliptical scattering spectra in SANS (Fig. 5B). Interestingly, anisotropy is observed in all but the most weathered shallow samples (SSRT5 and SPRT5; Fig. 5A). This indicates that the pores in the shale have a preferred orientation. All the chips are elongated in a direction perpendicular to the short axis in SANS spectra, indicating that the long axes of such pores are aligned with the long axes of the shale chips.

Connectivity:

Samples soaked in the D_2O-H_2O mixture had a much higher incoherent scattering background than the dry samples (because of the increased hydrogen incoherent scattering), making data at high Q difficult to interpret. Thus, we focused on USANS data and only the low-Q range of SANS data where the background was low (< 0.01 $Å^{-1}$). The I(Q) curves of four samples before and after the contrast-matching experiments are presented in Figure 6. The scattering curves for the least weathered bedrock sample analyzed with contrast matching (DC620) are almost identical before and after soaking in the D_2O-H_2O mixture, indicating that none of the pores in the measured size range are connected (Fig. 6A). In contrast, the slightly weathered shale bedrock chip (DC40) and more weathered soil chip (SSRT27) had some connected porosity at all measured Q values (Figs. 6B, C). Then, in a reverse, for the most intensively weathered shale

analyzed with contrast matching (SSRT5), pores were only connected in the smaller Q range, suggesting most of the smaller pores are closed (Fig. 6D).

The extent of pore connectivity was evaluated quantitatively by comparing calculated porosities for dry and soaked samples for Q values within the range $0.00003 < Q < 0.01$ $Å^{-1}$ (Table 2, Fig. 6E). Because of the narrower Q range due to high incoherent background in the contrast matching experiments, the porosity summarized here is lower than that calculated over the full experimental range (Table 1). Regardless, total porosity increases with more weathering. Consistent with I(Q) curves, the largest connected porosity is observed in SSRT5 (5.0%), followed by SSRT27 (4.1%), DC40 (2.5%) and DC620 (0%). The unconnected porosities are noticeably constant for the relatively unweathered samples (around 2%). Intriguingly, however, more unconnected pores were observed in the chip derived from the shallowest soil, SSRT5, than in the deeper drilled samples. Figure 6E emphasizes this point: i.e., unconnected porosity decreased with weathering only until the very surface chip, while connected porosity increased with weathering in all chips.

Ferrous and total iron:

The total iron contents of drilled core sediments were around 5.5 wt%, slightly higher than those observed in the soils (Table 3; Fig. 4D). The ferrous iron, however, showed more variations with depth: Fe (II) equaled $\leq$4 wt% 22 m below ground surface, decreased with removal of ankerite, and then remained relatively constant at shallower depths (Fig. 4D).

SEM and TEM images:

SEM photomicrographs of the clays in less weathered shale (SSRT27) surround quartz grains (Fig. 7A). In contrast, pore structures in the most weathered sample, SSRT5, clearly show that loss of clays (e.g., illite) has produced large pores situated between the clay that remains and the chemically resistant quartz (Figs. 7A, B). The high porosity observed in the weathered samples is thus attributed to loss of clays. TEM photomicrographs show similar features but at much higher magnifications (Figs. 7C, D). For example, the open space in SSRT27 is mostly observed within the clay grains (Fig. 7C), whereas many pores surround the quartz in the intensively weathered sample (Fig. D). In SSRT5, the quartz surfaces are smoother than those of the clays.

4. DISCUSSION

Reaction fronts:

Rose Hill shale contains predominantly clay minerals (~ 54 wt.% illite and ~ 9 wt.% "chlorite") and quartz (34 wt.%) with some feldspar and Fe-oxide. The shale also contains highly variable amounts of minor carbonate present as the mineral ankerite. However, our geochemical and mineralogical analysis of the drill core from Shale Hills showed that ankerite is not present -- most likely lost to leaching – at depths > 22 m below the land surface (Jin et al., 2010). This hypothesized loss of ankerite was also demarcated by a decrease in ferrous iron content in the DC sediments (Fig. 4D). The reaction front, or depth interval over which ankerite varies and is therefore considered to be dissolving, lies between 22 and 24 m depth. While we cannot disprove the alternate interpretation that the variation in Fe, Mg, and Ca concentrations over this interval could be caused by local variations in carbonate content in the original shale, this latter interpretation is deemed less likely given that we have also observed similar chemistry versus depth at other locations in the watershed, albeit at different depths (unpub. data). Furthermore, if the chemistry change at 22 m depth were due to stratigraphic change instead of chemical reaction, we would have expected a change in the total Fe content of the drill core. Instead, total Fe remained constant but ferrous Fe varied with depth, as expected for a reaction front involving Fe oxidation during ankerite dissolution (Fig. 4D). Based on these interpretations, samples used for this study represent Rose Hill shale that was weathered to different degrees, but completely depleted with respect to carbonates in every case (Fig. 1B).

A second reaction front was also inferred from the rock chemistry and chip density. The chips from drill core from deeper than ~5-6 m represent shale bedrock that has not yet been depleted in Na and Ca. At all shallower depths, the bedrock is inferred to have lost plagioclase feldspar to dissolution, accompanied by a decrease of chip density (Jin et al., 2010; Fig. 1B). Depletion of plagioclase appears to continue from this depth up into the regolith.

Clay mineral reactions, documented to be occurring only within the regolith, involve both dissolution of "chlorite" and illite: these phases transform further to vermiculite and hydroxyl-interlayered vermiculite which break down to form more stable kaolinite and Fe-oxyhydroxide (Jin et al., 2010). The secondary kaolinite and Fe-oxyhydroxides, present in higher abundance at shallow depths of the regolith, are also known to be lost as particles greater than 1.3 μm in size (Jin et al., 2010). Chips from the soil profiles are more weathered than drill core samples, with those sampled from 10 cm below the ground surface the most intensively altered. SEM and TEM photomicrographs imaged on chips from 10 cm depth in the soil show the large amounts of void space left by loss of illite and chlorite (Figs. 7B, D).

Fractal dimensions and interfacial features:

The power law correlation between scattering intensity and scattering vector indicates Porod behavior of the pore-particle interface over certain Q ranges (Fig. 3; Radlinski, 2006). The slope of the linear portion of the log I vs. log Q plots reveal the scale invariance or fractal behavior of the distributions of scattering objects (Wong et al., 1986). Porod exponents between 3 and 4 indicate scattering from a surface fractal at the respective length scale. A value of 3 is consistent with a very rough surface whereas a value of 4 denotes a perfectly smooth surface. In contrast, exponents between 3 and 2 indicate mass fractality (Mildner and Hall, 1986; Mildner et al., 1986; Radlinski, 2006). Previous studies have demonstrated that some fresh rocks (sedimentary rocks: sandstones, shales, carbonates; igneous rocks: basalts and granites) are fractal over several orders of magnitude in size or spacing of scatterers (e.g., Mildner et al., 1986; Aharonov and Rothman, 1996; Radlinski et al., 1999; Navarre-Sitchler et al., 2010).

Among the minerals present in SSHO shales, clay minerals have much higher surface area per gram than quartz and feldspar. Therefore, the surface area of shale is dominated by clays. Neutrons mainly scatter at clay-pore interfaces, hence, pore features observed by neutron scattering dominantly reflect these interfaces. Clay minerals are therefore inferred to be the most likely source of the fractal behavior (Wong et al., 1986). Laboratory measurements and computer simulations have illustrated that the fractal dimensions at pore-grain interfaces of sedimentary rocks depend on interfacial features related to dissolution and precipitation (Aharonov and Rothman, 1996). Specifically, the fractal dimension was shown to increase with an increase in diagenetic alteration and with higher percentages of cementing materials infilling pore space (Thompson, 1991).

From our NS experiments, we conclude that fractality is also a common characteristic of weathered shale samples and that fractal dimensions change as a result of dissolution of clay minerals in the weathering environment. All the drilled core samples we have analyzed where only feldspar was dissolving show mass fractal behavior. The shift from mass fractals to surface fractals is not observed until about 15 cm deep, well above the bottom of the clay-weathering front (i.e. the depth where significant clay reactions initiate). With more clay dissolution, the mineral-pore interface becomes smoother (Fig. 4A), presumably due to exposure of smooth quartz surfaces. This depth also coincides with precipitation of kaolinite and Fe-oxyhydroxides (Jin et al., 2010). Thus the infiltrating fluids are presumed to be at equilibrium with those phases at those depths, perhaps consistent with more smooth mineral surfaces (White and Brantley, 2003).

Interestingly, although the slopes of the scattering curves change with weathering, there is no break in slope for any given shale sample. In contrast, our recent observations on weathering samples of crystalline granitic and basaltic rocks documented breaks in slope in the log I versus log Q curves (Navarre-Sitchler et al., 2010). In that work, the break in slope delineated two populations of scatterers: pores and bumps on surfaces. We argued that pores were generally situated at grain boundaries or triple junctions; therefore, the pore spacing was dictated by the grain size of the rock. Scattering at low Q occurred from micron-spaced pores, while scattering at high Q originated from submicron-sized bumps. Extrapolating from that study to this one, the lack of a break in slope in the shale plots may be because pores and bumps on surfaces are equivalent in shale since particles in shales are themselves micron- to submicron-sized.

The anisotropy of pores:

It is commonly observed that porosity in shales is anisotropic, with pores compressed in the direction perpendicular to the bedding, but symmetric within the bedding plane (Hall et al., 1983; Mildner, 1986; Allen, 1991). Neutron scattering and SEM micrographs of Rose Hill bedrock show that, even within the bedding, the pores are preferentially oriented (Figs. 5B, 7A). It is possible that these preferentially oriented and anisotropic pores may be related to the pencil cleavage that developed in the Rose Hill Formation associated with the formation of the Valley and Ridge province of Appalachian Mountains (Flueckinger, 1969). We also observed that the long axes of the pores coincide with the long axes of the rock chips. It is thus possible that the elongated rock fragments may form because of the prior formation of anisotropic pores which in turn may be related to the pencil cleavage.

Most of the water flowing through the unaltered bedrock probably follows bedding, pencil cleavage, or fractures. Along the rock-water interface at depth, first carbonates and then feldspars dissolve, contributing to growth of pre-existing cylindrical pores or creating new pores. Throughout the bedrock and regolith, the pores remain relatively anisotropic. The eccentricity of pores decreases with extent of weathering. Eventually, pores become nearly isotropic in the most weathered shale chips recovered from the shallowest soil (SSRT5 and SSRT27 at10 cm below surface). Pore anisotropy is lost only when clay minerals disappear to a significant extent and the mineralogy becomes dominated by quartz (Fig. 5).

Variation in porosity and surface area as weathering progresses:

The observed shifts from mass to surface fractal and from rough to smooth surface with increasing intensity of weathering are accompanied by changes in porosity and specific surface

area (SSA) (Figs. 4B, C). The porosity that can be measured with NS in the Rose Hill bedrock is about 5-6 %, and most of this is unconnected and thus inaccessible to water (Fig. 6E). The NS measurements reported here were all completed on chips collected above the hypothesized carbonate weathering front in the drilled core (Figs. 1B, 4D; Jin et al., 2010). Thus, if this carbonate concentration-depth dependence is indeed a weathering reaction front, then the carbonate that was dissolved out of the bedrock above 22 m was presumably originally present only in layers or zones between carbonate-free layers or zones. The chips studied with NS presumably derive from the noncarbonate-containing layers and zones.

The porosity remains unchanged in drill core chips collected 5 m below ground. It then increases towards surface and reaches ~9% at about 1 m. Of this, 4% is considered secondary and 5% primary porosity. Secondary pores are partly connected (Fig. 6E). The most consistent interpretation of these data is that a zone with a high density of fractures or pores has formed in the uppermost 5 m beneath the land surface. This interpretation is consistent with the depth distribution of shale chip densities that show large variation in the uppermost 5-6 m (Jin et al., 2010). It is highly likely that the loss of Na and Ca in plagioclase in this zone either caused new fractures or pores or was caused by the emplacement of fractures and pores that decreased the chip bulk density (Jin et al., 2010).

If plagioclase dissolution postdated the growth of such porosity, it is possible that the higher porosity was caused by physical disaggregation associated with annual freeze - thaw cycles. Such processes could be ongoing today, but could also have been particularly intense during periglacial climate conditions at approximately 15 ky ago (Gardner et al., 1991). Rock fractures are known to originate from ice-segregation and frost wedging (Murton et al., 2006; Matsuoka and Murton, 2008). This process may be especially important in periglacial climates, where daily air temperatures fluctuate above and below the freezing point. The SSA in chips derived from 1-4 m depth in this saprock zone is also much higher than that of the underlying bedrock, reaching up to 120 m^2/g (Fig. 4C). Again, it is likely that this higher surface area is related to new fractures or pores as well as the weathering of feldspar. The importance of feldspar dissolution as a major reaction associated with the conversion of bedrock to saprock while creating porosity and surface area has been noted in other weathering systems (Brantley and White, 2009; Navarre-Sitchler et al., 2010).

The mineral reaction that is most closely associated with the disaggregation of saprock and formation of regolith is clay dissolution. Significant clay reactions begin centimeters below the saprock-regolith interface (Jin et al., 2010). These reactions contribute to the growth in porosity to 16% as observed in shale chips from 10 cm depth. Eventually, with further

weathering, the fractal dimension shifts above 3 (Fig. 4A). The two soil profiles are similar in porosity and fractal dimension, suggesting that our observations may be representative of ridge sites (Fig. 4).

Of the total porosity in samples from shallow depths, half is contributed by unconnected pores while the other half is connected. However, more unconnected pores were observed in chips recovered from 10 cm depth than existed as primary pores in the bedrock. Contrast matching experiments also suggested that most of the smaller pores are unconnected (Fig. 6). These unconnected pores cannot be produced by dissolution, since water by definition is not flowing through unconnected pores. The formation of secondary phases such as kaolinite in chips in the soils could trap unconnected pores, limiting accessibility to water. Mineralogical studies have documented greater abundances of kaolinite and Fe-oxyhydroxides in shallower soils (Jin et al., 2010). Alternatively, freeze-melt cycles could also have formed unconnected stress-induced fractures or pores given the large seasonal fluctuations of soil temperature at 10 cm.

Shale chips in the shallow soils have lower SSA values than medium depth soil chips: this SSA is comparable to that of bedrock (Fig. 4C). Two processes could potentially lead to the loss of surface area, even as porosity increases: 1) smaller pores connect to produce larger pores by dissolving the mineral walls between them; and 2) bumps on surfaces of pores dissolve away. Either process smoothes the internal surface of the rock, and explains the increase in fractal dimension from about 3 to 4 over the same interval that the porosity begins to decrease. Both processes could be occurring due to dissolution of primary chlorite and illite to leave smoother quartz grains (Fig. 7).

Conceptual models for pore development and shale weathering:

Allen (1991) categorized the pores within shales into three types based on their size and fractal behaviors (Fig. 8). Type I consists of interlayer pores that lie between stacked clay layers. These interlayer pores are characterized by diameters of only Ångstroms, and are thus not detectable by SANS/USANS. Type II porosity is comprised of intraparticle pores that define a three-dimensional network within the clay grains and that exhibit mass fractals. The fine clay structure of type II pores contributes to the larger, interparticle pores of type III, which exhibit surface fractals. Thus, the scattering features in Rose Hill shale associated with unweathered or only slightly weathered samples (DC40, DC160, DC540, DC620, DC1990, SSRT27 and SPRT25) are probably dominated by type II pores. The distribution of their size or separation is best described as a mass fractal. As weathering intensifies, the shale chips develop pores that are

best described by a surface fractal with smoother grain-pore interfaces (Fig. 4B). Such interparticle pores (type III) are also documented by SEM and TEM imaging (Figs. 7B, D).

In summarizing these observations, we propose the following sequence for generation of porosity and change in specific surface area above the carbonate reaction front (Fig. 9). Within the bedrock, pores are intraparticle, unconnected and anisotropic, and they are characterized as mass fractals (Fig. 9A). It is very possible that these pores are related to the pencil cleavage that characterizes this rock since many shales do not have anisotropic porosity.

At about ~ 6 m below land surface, feldspar dissolution initiates, leading to creation of connected anisotropic pores and increased water-accessible mineral surface area. Porosity increases throughout this zone and within centimeters of the bedrock-regolith interface, the chemistry of the rock chips document significant clay dissolution reactions. At this point, the porosity still comprises a mass fractal, albeit with a fractal dimension close to 3. As clay grains dissolve and intraparticle pores connect to produce interparticle pores, the porosity transforms to a surface fractal (Figs. 7B, 9B, 9D). The fractal dimension of 3-3.2 is consistent with a mineral-pore interface that is bumpy. This nm to μm-scale roughness is presumably controlled by surface features such as the density of etch pits at defects, steps, and grain boundary outcrops on the dissolving surface. Further loss of clay minerals and exposure of quartz, however, lead to further increases in porosity, a higher fractal dimension, and a decrease in pore anisotropy. Kaolinite and Fe-oxyhydroxide also precipitate in the shallower soils (~ 10 cm below ground). Eventually a lower surface area develops in the top-most samples as small pores are connected to form large pores, pore surface bumps are dissolved away, or secondary mineral precipitates smooth over bumps. The latter process is also the likely explanation for how some unconnected pores are created in the shallowest sample (Fig. 9C).

Chemical processes driving shale weathering and soil formation at Shale Hills

At Shale Hills, physical, biological and chemical reactions could all contribute to the transformation of bedrock to regolith (Fig. 9D). However, it is also possible that the bedrock alters to regolith predominantly due to chemical reactions. For example, the changes in chemistry and porosity between bedrock and weathered saprock were observed at 22 m below land surface, well below the point where the rock temperature fluctuates significantly on a daily or seasonal basis. Furthermore, roots are only rarely present at such depths (e.g., Idso and Kimball, 1991). Thus, the advance of the bedrock-saprock interface is most likely largely due to dissolution of the reactive carbonate mineral ankerite.

Dissolution of trace amounts of calcite has also been shown to be critical in initiating soil formation on granites (White et al., 2005). Another reaction that is commonly observed to influence the initiation of rock weathering in other systems is volume expansion during oxidative weathering of ferrous phyllosilicates in weathering granites (Fletcher et al., 2006; Buss et al. 2008). Likewise, the ankerite dissolution front in the Rose Hill shale is the depth interval where Fe(II) in the ankerite is oxidized to Fe(III) (Figs. 9D, 4D). Thus, both acids and oxidants are important reactants at the bedrock-saprock interface in this rock.

However, that dissolution reaction can only proceed if water is flowing through the rock at depth. Given the limited pore connectivity and geometry of the Rose Hill Formation, we argue that advective water flow dominates parallel to the ankerite weathering fronts or along the fratures, but transport of these reactants (and water) into this low-porosity and low-permeability bedrock, or transport of products out is dominated by diffusion (Fig. 9D; e.g., Jardine et al., 1999). Therefore, solutes in the bedrock have a long residence time and the rate of advance of the bedrock/saprock interface is limited by water transport processes (Meunier et al., 2007). Under these conditions, small changes in porosity will have a major influence on water flowpaths and thus the weathering advance rate. The neutron scattering techniques are shown to be sensitive to mineral-pore interface, thus able to detect any new surface area created during chemical weathering processes. Using NS to document the location of the reaction front where porosity grows should allow predictive understanding of weathering advance.

5. CONCLUSIONS AND IMPLICATIONS

We investigated shale weathering at the Susquehanna Shale Hills Critical Zone Observatory using neutron scattering techniques coupled with electron microscopy and detailed chemical and mineralogical interrogation. We showed that the changes in physical properties (e.g., porosity, surface area) and mineralogy and chemical composition occur in depth-related patterns that can be correlated. Ankerite is the first mineral to dissolve at depth and the reaction front for this mineral is used to define the bedrock-saprock interface. Ankerite, inferred to be present mostly as cement between carbonate-poor zones or layers, is completely depleted at a depth of 22 m below ground surface. Dissolution of ankerite is accompanied by oxidation of Fe (II) to Fe (III).

Starting around 5 m below ground surface, the porosity in the saprock significantly increases, either due to feldspar dissolution or to ice-wedging during the periglacial period. At shallower depths but still in the saprock, clay dissolution starts, and is accompanied by an increase in porosity. Within centimeters of the onset of clay dissolution, the saprock transforms to

regolith that can be hand-augered. At about 15 cm below land surface within the regolith, clays have been weathered to an extent that shale chips experience a transition: pores in the chips that are described at depth as mass fractals shift to surface fractals because intraparticle pores connect to produce interparticle pores. Pores in the unweathered shale are anisotropic but become more symmetric with clay dissolution. The mineral-pore interface becomes smoother, causing the surface area to decrease in the regolith. This smoothing is largely a result of exposure of quartz surfaces and precipitation of secondary kaolinite and Fe-oxyhydroxide. These precipitation reactions as well as temperature fluctuations accompanying freeze-thaw cycles create unconnected pores at this shallow depth.

The size distribution and physical connectivity of pores within rocks and soils control chemical dissolution pathways by influencing both exposed surface area and water-accessible flow pathways. The primary porosity at Rose Hill shale is only 5% and is mostly unconnected, indicating that diffusion and fluid transport limit chemical dissolution reactions and bedrock-saprolite conversion rates. To our knowledge this study is one of the first of its kind to use of small-angle neutron scattering to investigate weathering rocks at field scales (Navarre-Sitchler et al., 2010).

Acknowledgements:

We acknowledge instrumentation and technical support at NCNR-NIST from Andrew Jackson and Rick Paul. John Cantolina at Material Characterization Laboratory at the Pennsylvania State University helped with SEM. This work utilized facilities supported in part by the National Science Foundation under Agreement No. DMR-0454672.We acknowledge the support of the National Institute of Standards and Technology, U.S. Department of Commerce, in providing the neutron research facilities used in this work. GR and DRC are supported from the U.S. Department of Energy, Office of Basic Energy Sciences through 'Structure and Dynamics of Earth Materials, Interfaces, and Reactions' (FWP ERKCC72) under contract DE-AC05-00OR22725 to Oak Ridge National Laboratory, managed and operated by UT-Battelle, LLC. LJ and SLB acknowledge funding from NSF CHE-0431328 (PI: S. Brantley) for support for the Environmental Molecular Sciences Institute at Penn State (Center for Environmental Kinetics Analysis) and from NSF EAR-0725019 (PI: C. Duffy, Penn State) for the Susquehanna/Shale Hills Critical Zone Observatory. Logistical support was provided by the NSF-supported Shale Hills Susquehanna Critical Zone Observatory.

Figure captions:

Figure 1: A) Sampling locations in the Shale Hills catchment (modified from Lin et al., 2007; Jin et al., 2010). Background color indicates regolith thickness. DC1 is the drill core site, where 25 meters of parent shale were drilled and samples as chips and powder. Soil cores SPRT and SSRT were collected at the ridge top at two locations on the north-facing slope. B) Sample depths

shown relative to the weathering fronts for primary minerals as documented by major element chemistry (Jin et al., 2010).

Figure 2: Absolute neutron scattering intensity plotted as a function of scattering vector for sample DC160. Data shown are combined from small-angle neutron scattering (SANS) and ultra small-angle neutron scattering (USANS).

Figure 3: Scattering curves for samples from the drill core (DC1, A), and two soil profiles (SSRT, B; SPRT, C). Notice that the shales that are more intensively weathered scatter neutrons more strongly.

Figure 4: Variations of power law Porod exponent (A), porosity (B), specific surface area (C), and ferrous and total Fe contents as a function of depth (D), for shales that have been weathered to different extents. The exponent, *n*, indicates the type of fractal ($2 < n < 3$, mass fractal; $3 < n < 4$, surface fractal).

Figure 5: Raw data from the SANS detector for SSRT5 (A) and SSRT15 (B). The distance from the scattering profile center is proportional to the scattering vector Q, and the colors indicate the relative intensity, with warm colors indicating higher intensity. Note that pores in SSRT5 appear to have no preferred direction, whereas those in SSRT15 are anisotropic.

Figure 6: Scattering curves for unweathered (DC260, A), slightly weathered (DC40, B; SSRT27, C) and intensively weathered (SSRT5, D) shales, in dry (solid diamond) and wet (open circle) conditions. The scattering of neutrons in dry samples is from all pores (connected and unconnected), whereas in wet samples it is only from unconnected pores. The difference between the two curves is therefore attributed to connected pores. The total and unconnected porosities were calculated for these four shales (E).

Figure 7: Images from scanning electron microcopy for slightly weathered (SSRT27, A) and intensively weathered (SSRT5, B) shale chips recovered from regolith. Notice the fibre-like texture of the shale that controls the anisotropic nature of the pores. The black arrows point to the pores, which could be intraparticle pores within the shale grains or interparticle pores between quartz and clay grains. Images from transmission electron microcopy for slightly weathered (SSRT27, C) and intensively weathered chips (SSRT5, D). Circles indicate where EDS measurements were completed, where areas A, C, D are consistent with quartz and areas B, E, F with clay minerals. Area F is partly a pore as indicated by presence of Cu in the spectrum.

Figure 8: Three types of pores present in the shales (modified from Allen, 1991). See text for details.

Figure 9: A schematic diagram summarizing the production and changes in connectivity of the pores as measured by NS, and the processes that are causing changes in porosity at different depths. Initially, shales are dominated by unconnected type II pores (A). With weathering, pores become more connected by loss of clays and type III pores dominate (B). With progressive weathering, more space opens up due to clay dissolution, which exposes the quartz (C). Precipitation of kaolinite (K) likely clogs some pores, making them partly inaccessible to water. Processes of physical weathering such as freeze-melt cycling could also create new unconnected pores. At Shale Hills, chemical, physical and biological processes all can contribute to regolith formation and pore production (D). Depletion of major elements illustrates three weathering fronts at different depths (ankerite, feldspar, and clays), as seen by the negative $\tau_{Zr,j}$ values (Jin et al., 2010). Water flows in the saprock and regolith dominated by advection along the

bedrock/saprock interface and along fractures, but by diffusion into the grains and into the bedrock. See text for details.

References:

Agamalian M., Carpenter J.M. and Richardson J.W. (2009) Validity of the Darwin and Ewald reflectivity functions in the range of the far wings: Neutron diffraction study. *Physics Letter A* **373**, 292-295.

Aharonov E. and Rothman D.H. (1996) Growth of correlated pore-scale structures in sedimentary rocks: A dynamical model. *Journal of Geophysical Research* **101**, 2973-2987.

Allen A. J. (1991) Time-resolved phenomena in cements, clays and porous rocks. *Journals of Applied Crystallography* **24**, 624-634.

Anderson, S.P. (2005) Glaciers show direct linkage between erosion rate and chemical weathering fluxes. *Geomorphology* **67**, 147-157.

Anderson, S. P., von Blanckenburg, F., and White, A. F. (2007) Physical and chemical controls on the Critical Zone. *Elements* **3**, 315-319.

Avnir D., Farin D., and Pfeipfer P. (1984) Molecular fractal surfaces. *Nature* **308**, 261.

Anovitz L.M., Lynn G.W., Cole D.R., Rother G., Allard L.F., Hamilton W.A., Porcar L. and Kim M. (2009) A new approach to quantification of metamorphism using ultra-small and small angle neutron scattering. *Geochim. et Cosmochim. Acta*, **73**, 7303-7324.

Barker J.G., Glinka C.J., Moyer J.J., Kim M.H., Drews A.R. and Agamalian M. (2005) Design and performance of a thermal-neutron double-crystal diffractometer for USANS at NIST. *J Appl. Cryst*. **38(6)**, 1004-1011.

Bragg W.L. (1913) The diffraction of short electromagnetic waves by a crystal. Proceedings of the Cambridge Philosophical Society 17, 43-57.

Brantley S. L., and White A. F. (2009) Approaches to modeling weathered regolith. *Reviews in Mineralogy and Geochemistry* **70**, 435-484.

Brantley S. L., White T. S., White A.F., Sparks D., Richter D., Prgitzer, K., Derry L., Chorover J., Chadwick O., April R., Anderson S., Amundson R. (2006). Frontiers in exploration of the Critical Zone: Report of a workshop sponsored by the National Science Foundation (NSF), October 24-26, 2005, Newark, DE, 30pp.

Buss H. L, Bruns M. A., Schultz M. J. Moore J, Mathur C. F., Brantley S. L. (2005) The coupling of biological iron cycling and mineral weathering during saprolite formation, Luquillo Mountains, Puerto Rico. *Geobiology* **3**, 247-260.

Buss H. L., Sak P. B., Webb S. M., and Brantley, S. L. (2008) Weathering of the Rio Blanco quartz diorite, Luquillo Mountains, Puerto Rico: Coupling oxidation, dissolution, and fracturing. *Geochim. et Cosmochim. Acta*, **72**, 4488-4507.

Cole D.R., Mamontov E. and Rother, G. (2009) Structure and dynamics of fluids in microporous and mesporous Earth and engineered materials. In: Neutron applications in Earth, energy, and environmental sciences, L. Liang, R. Rindaldi and H. Schober, Springer Verlag.

Cox N. J. (1980) On the relationship between bedrock lowering and regolith thickness. *Earth Surface Processes* **5**, 271-274.

Dietrich W.E. and Perron J.T. (2005) The search for a topographic signature of life. *Nature* **439**, 411-418.

Failey M. P., Anderson D. L., Zoller W.H., Gordon G.E., and Lindstrom R. M. (1979) Neutron-capture prompt γ-ray activation analysis for multielement determination in complex samples. *Analytical Chemistry* **51**, 2209-2221.

Fletcher R. C., Buss H. L. and Brantley S.L. (2006) A spheroidal weathering model coupling pore-water chemistry to soil thicknesses during steady state weathering. *Earth and Planetary Sci. Letters* **244**, 444-457.

Flueckinger L.A. (1969) Geology of a portion of the Allensville Quadrangle, Centre and Huntingdon Counties, Pennsylvania, PA. Topographic and Geological Survey Progress Report.

Folk R.L. (1960) Peterography and origin of the Tuscarora, Rose Hill, and Keefer Formations, Lower and Middle Silurian of eastern west Virginia. *Journal of Sedimentary Petrology* **30**, 1-58.

Gabet E.J., Reichman O.J., Seabloom E.W. (2003) The effects of bioturbation on soil processes and sediment transport. *Annual Review of Earth and Planetary Sciences* **31**, 249-273.

Glinka C.J., Barker J.G., Hammouda B., Krueger, S., Moyer, J.J. and Orts, W.J. (1998) The 30 m Small-Angle Neutron Scattering Instruments at the National Institute of Standards and Technology. *J Appl. Cryst.* **31(3),** 430.

Gardner T.W., Ritter J.B., Shuman C.A., Bell J.C., Sasowsky K.C. and Pinter N. (1991) A periglacial stratified slope deposit in the valley and ridge province of central Pennsylvania, USA: Sedimentology, stratigraphy, and geomorphic evolution. *Permafrost and Periglacial Processes* **2**, 141-162.

Goldich S.S. (1984) Determination of ferrous iron in silicate rocks. *Chemical Geology* **42**, 343-347.

Graham G.C., Rossi A.M. and Hubbert K.R. (2010) Rock to regolith conversion: production hospitable substrates for terrestrial ecosystems. *GSA today* **20 (2)**, doi: 10.1130/GSAT57A.1.

Green, E.G., Dietrich, W.E. and Banfield J.F. (2006) Quantification of chemical weathering rates across an actively eroding hillslope. *Earth and Planetary Science Letters* **242**, 155-169.

Guinier A. and Forner G. (1955) Small-angle scattering of X-rays; Wiley: New York, 1955.

Hall P.L., Mildner D.F.R. and Borst, R.L. (1983) Pore size distribution of shaly rock by small angle neutron scattering. *Appl. Phys. Lett.* **43**, 252-254.

Heimsath, A. M., Dietrich, W. E., Nishiizumi, K. and Finkel, R. C. (1997) The soil production function and landscape equilibrium. *Nature* **388**, 358-361.

Hinde, A.L. (2004) PRINSAS- a Windows-based computer program for the processing and interpretation of small-angle scattering data tailored to the analysis of sedimentary rocks. *Journal of Applied Crystallography* **37**, 1020-1024.

Idso S.B. and Kimball B.A. (1991) Effects of two and a half years of atmospheric CO_2 enrichment on the root density distribution of three-year-old sour orange trees. *Agircultural and Forest Meterolog*y **55**, 345-349.

Jardine P.M., Sanford W.E., Gwo J.P., Reedy O.C., Hicks D.S., Riggs J.S. and Bailey W. (1999) Quantifying diffusive mass transfer in fractured shale bedrock. *Water Resource Research* **35 (7),** 2015-2030.

Jin L., Williams E.L., Szramek K.J., Walter L.M. and Hamilton S.K. (2008) Silicate and carbonate mineral weathering in soil profiles developed on Pleistocene glacial drift (Michigan, USA): Mass balances based on soil water chemistry. *Geochim. Cosmochim. Acta* **72**, 1027-1042.

Jin L., Ravella R., Ketchum B., Bierman P.R., Heaney P., White T. and Brantley S.L. (2010) Mineral weathering and elemental transport during hill slope evolution at the Susquehanna Shale Hills Critical Zone Observatory. In press for *Geochim. Cosmochim. Acta.*

Jongmans A.G., van Breemem N., Lundstrom, U., van Hees, P.A.W., Finlay R.D., Srinivasan M., Unestam T., Giesler R., Melkerud P.A. and Olsson M. (1997) Rock-eating fungi. *Nature* **389**, 682-683.

Kahle A., Winkler B., Radulescu A. and Schreuer J. (2004) Small-angle neutron scattering study of volcanic rocks. *Euro. J. Miner.* **16**, 407-417.

Kline S. R. (2006) Reduction and Analysis of SANS and USANS Data using Igor Pro. *J Appl. Cryst.* **39(6)**, 895.

Krohn C.E. (1988) Sandstone fractal and Euclidean pore volume distributions. *J. Geophy. Research* **93**, 3286-3296.

Lin H. and Zhou X. (2008) Evidence of subsurface preferential flow using soil hydrologic monitoring in the Shale Hills catchment. *European Journal of Soil Science* **59**, 34-49.

Lucido G., Tiolo R. and Caponetti E. (1988) Fractal approach in petrology: small-angle neutron scattering experiments with volcanic rocks. *Phys. Rev*. B **38**, 9031-9034.

Lynch J.A. and Corbett E.S. (1985) Source-area variability during peak flow, edited by E.B. Jones and T.J. Ward, J. Irrig. Drain. Div. Am. Soc. Civ. Eng., pp. 300-307., in Watershed Management in the 1980s, E. Jones and T. Ward, Editors. ASCE: Reston, VA. p. 300-307.

Ma L., Chabaux F., Pelt E., Blaes E., Jin L., and Brantley S.L. (2010) Regolith production rates calculated with Uranium-series isotopes at Susquehanna Shale Hills Critical Zone Observatory. In review for *Earth and Planetary Science Letters*.

Matsuoka N. and Murton J. (2008) Frost weathering: recent advances and future directions. *Permafrost and Periglacial Processes* **19**, 195-210.

McFadden L.D., Eppes M.C., Gillespie A.R. and Hallet B. (2005) Physical weathering in arid landscape due to diurnal variation in the direction of solar heating. *Geological Society of America Bulletin* **117 (1/2)**, 161-173.

Merino E., Nahon, D. and Wang, Y. (1993) Kinetics and mass transfer of pseudomorphic replacement: Application to replacement of parent minerals and kaolinite by Al, Fe, and Mn oxides during weathering. *American Journal of Science* **293**, 135-155.

Meunier A., Sardini P., Robinet J. C. and Pret D. (2007) The petrography of weathering processes: facts and outlooks. Clay Minerals 42, 415-435.

Mildner D. F. R. and Hall P. L. (1986) Small-angle scattering from porous solids with fractal geometry. *J. Phys. D: Appl. Phys.* **19**, 1535-1545.

Mildner D. F. R., Rezvani R., Hall P.L. and Borst R.L. (1986) Small-angle scattering of shaly rocks with fractal pore interfaces. *Appl. Phys. Lett.* **48**(19), 1314-1316.

Minasny B. and McBratney A. B. (1999) A rudimentary mechanistic model for soil production and landscape development. *Geoderma* 90, 3-21.

Molnar P., Anderson R.S. and Anderson S.P. (2007), Tectonics, fracturing of rock, and erosion, *J. Geophys. Res.,* 112, F03014.

Murton J. B., Peterson R., Ozouf J. C. (2006) Bedrock fracture by ice segregation in cold regions. *Science* **314**, 1127-1139.

Navarre-Sitchler A., Steefel C.I., Yang L. and Tomutsa L. (2009) Evolution of porosity and diffusivity associated with chemical weathering of a basalt clast. *Journal of Geophysical Research - Earth Surface*, doi:10.1029/2008JF001060.

Navarre-Sitchler A., Jin L., Rother, G., Cole, D.R., Buss, H. and Brantley S.B. (2010) How nanoporosity and microporosity grow in weathering rocks. In review for *Nature-Geosciences.*

Oguchi C. T. (2004) A porosity-related diffusion model of weathering-rind development. *Catena* **58**, 65-75.

Pernyeszi T. and Dekany I. (2003) Surface fractal and structural properties of layered clay minerals monitored by small-angle X-ray scattering and low-temperature nitrogen adsorption experiments. *Colloid Polym. Sci.* **281**, 73-78.

Porod G (1952) Die Röntgenkleinwinkelstreuung von dichtgepackten kolloiden Systemen. II Teil. Kolloid Z 125:51-57, 108-122.

Radlinski A.P., Ioannidis M.A., Hinde A.L., Hainbuchner M., Baron M., Rauch H. and Kline S.R. (2004) Angstrom-to-millimeter characteriation of sedimentary rock microstrcture. *J. of Colloid and Interface Sci.* **274**, 607-612.

Radlinski A. P. (2006) Small-angle neutron scattering and the microstructure of rocks. In *Neutron Scattering in the Earth Sciences, v. 31*, Vol. 63, pp. 363-397.

Radlinski A.P., Radlinska E.Z., Agamalian M., Wignall G.D., Lindner P. and Randl O.G. (1999) Fractal geometry of rocks. *Physical Review Letters* **82**, 3078-3081.

Roering J.J., Almond P., Tonkin P., McKean J. (2002) Soil transport driven by biological processes over millennial time scales. *Geology* **30**, 1115-1118.

Rossi A.M. and Graham R.C. (2010) Weathering and porosity formation in subsoil granitic clasts, Bishop Creek moraines, California. *Soil Science Society of American Journals* **74(1)**, 172-185.

Royne A., Jamtveit B., Mathiesen J. and Malthe-Sorenssen A. (2008) Rock weathering rates by reaction-induced hierarchical fracturing. *Earth and Planetary Science Letters*, **275**, 364-369.

Sak P.B., Fisher D.M., Gardner T.W., Murphy K. and Brantley S.L. (2004) Rates of weathering rind formation on Costa Rican basalt. *Geochimica et Cosmochimica Acta* **68**, 1453-1472.

Schaetzl R.J. and Anderson S. (2005) Soils: Genesis and Geomorphology. New York: Cambridge University Press, 817pp.

Smucker A.J.M., Park, E., Dorner J. and Horn R. (2007) Soil micropore development and contributions to soluble carbon transport within macroaggregates. *Vadoze Zone Journal*, **6**, 282-290.

Stevenson F.J. and Cole M. A. (1999) Cycles of soils: carbon, nitrogen, phosphorus, sulfur, micronutrients. New York, Willey, 2nd Edition.

Tan K.H. (2003) Humic matter in soil and environment: Principles and controversies. Marcel Dekker, New York.

Thompson A.H. (1991) Fractals in rock physics. *Annual Rev. Earth Planet. Sci.* **19**, 237-262.

van Breemen N., Lundstrom U.S. and Jongmans A.G. (2000) Do plants drive podzolization via rock-eating mycorrhizal fungi? *Geoderma* **94**, 163-171.

White A.F. and Brantley S.L. (2003) The effect of time on the weathering of silicate minerals: why do weathering rates differ in the laboratory and field? *Chemical Geology* **202**, 479-506.

White A.F., Schulz M.S., Lowenstern J.B., Vivit, D.V. and Bullen T.D. (2005) The ubiquitous nature of accessory calcite in granitoid rocks: Implications for weathering, solute evolution, and petrogenesis. *Geochimica et Cosmocimica Acta* **69 (6)**, 1455-1471.

White A.F., Schulz M.S., Stonestrom D.A., Vivit D.V., Fitzpatrick J., Bullen T.D. Maher K. and Blum A.E. (2009) Chemical weathering of a marine terrace chronosequence, Santa Cruz, California. PartII: Solute profiles, gradients and the comparisons of contemporary and long-term weathering rates. *Geochim. Cosmochim. Acta* **73**, 2769-2803.

Wong P., Howard J. and Lin J.-S, (1986) Surface roughening and the fractal nature of rocks. *Phys. Rev. Lett.* **57**, 637-640.

Yoo K., Mudd S.M., Sanderman J., Amundson R. and Blum, A.E. (2009) Spatial patterns and controls of soil chemical weathering rates along a transient hillslope. *Earth and Planetary Science Letters* **288**, 184-193.

Figure 1A.

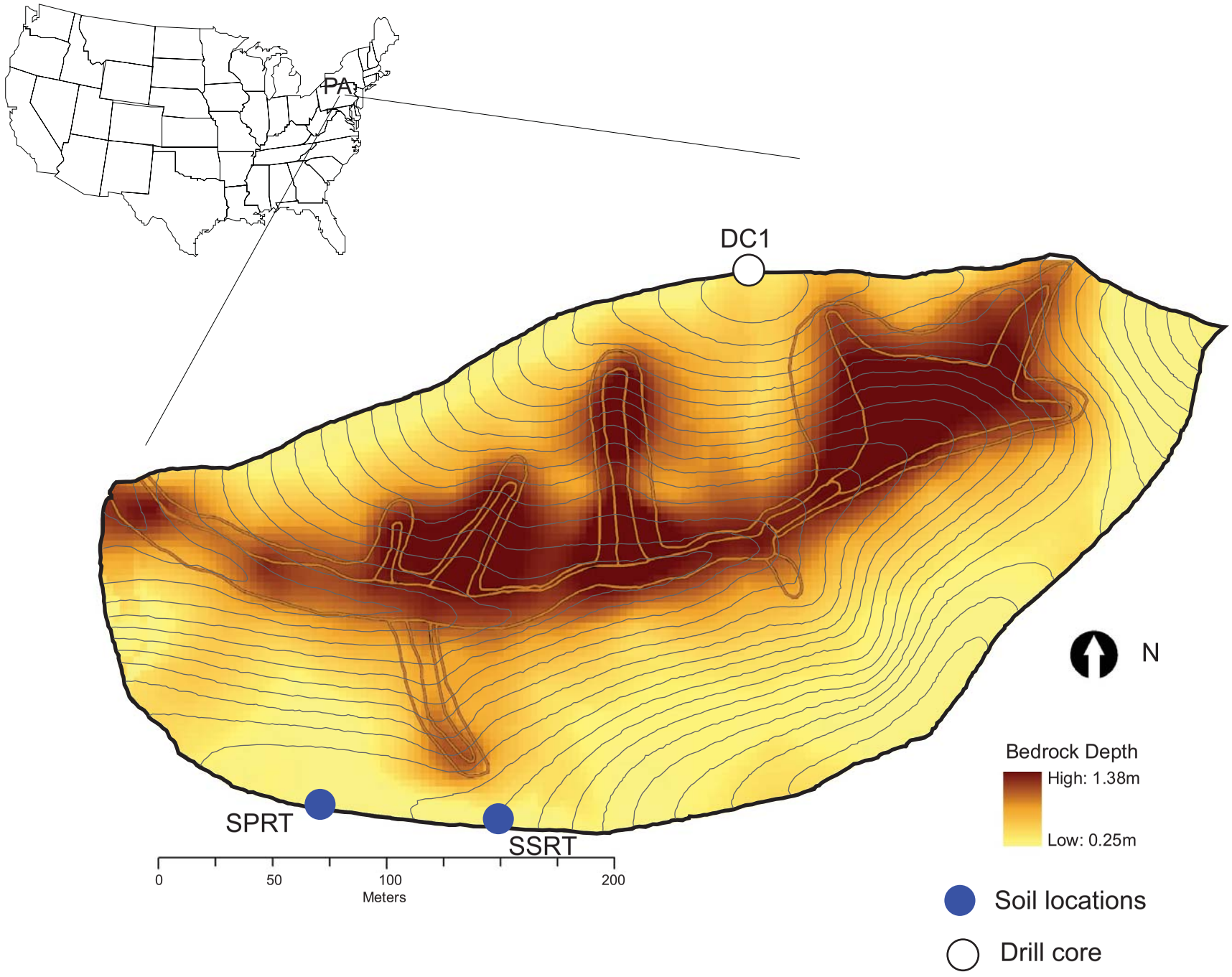
PA
DC1
SPRT
SSRT
0
50
100
200
Meters
N
Bedrock Depth
High: 1.38m
Low: 0.25m
Soil locations
Drill core

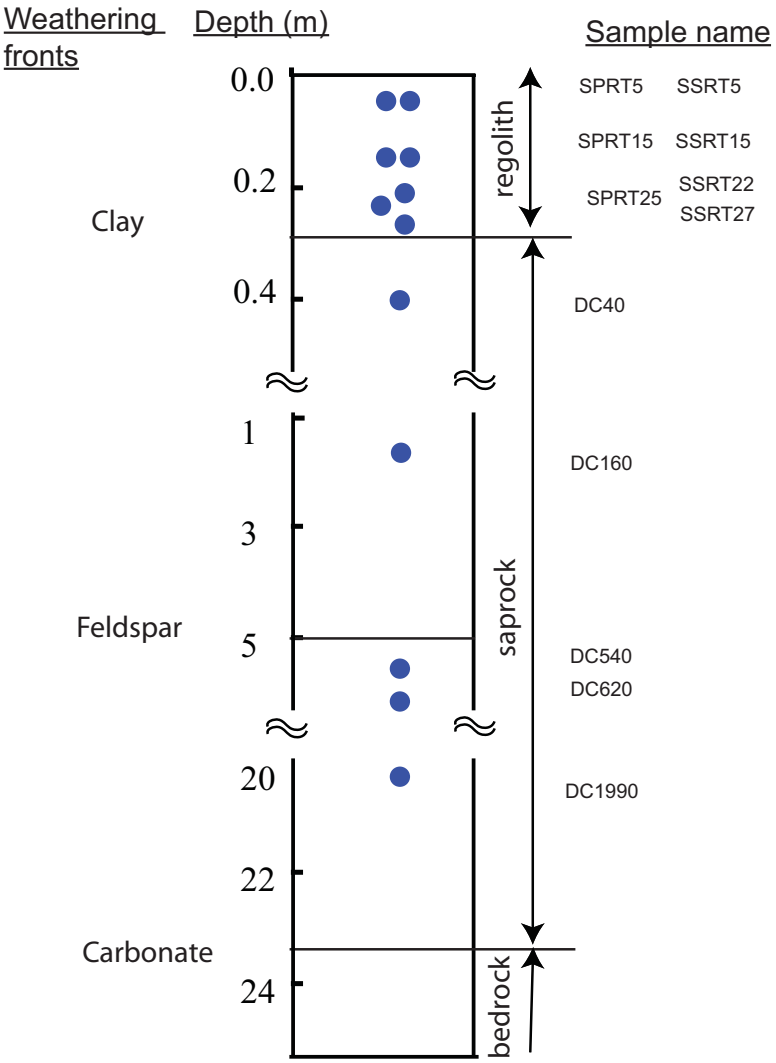
Weathering fronts
Depth (m)
Sample name
0.0
0.2
0.4
1
3
5
20
22
24
Clay
Feldspar
Carbonate
regolith
saprock
bedrock
SPRT5
SSRT5
SPRT15
SSRT15
SPRT25
SSRT22
SSRT27
DC40
DC160
DC540
DC620
DC1990

Figure 1B.

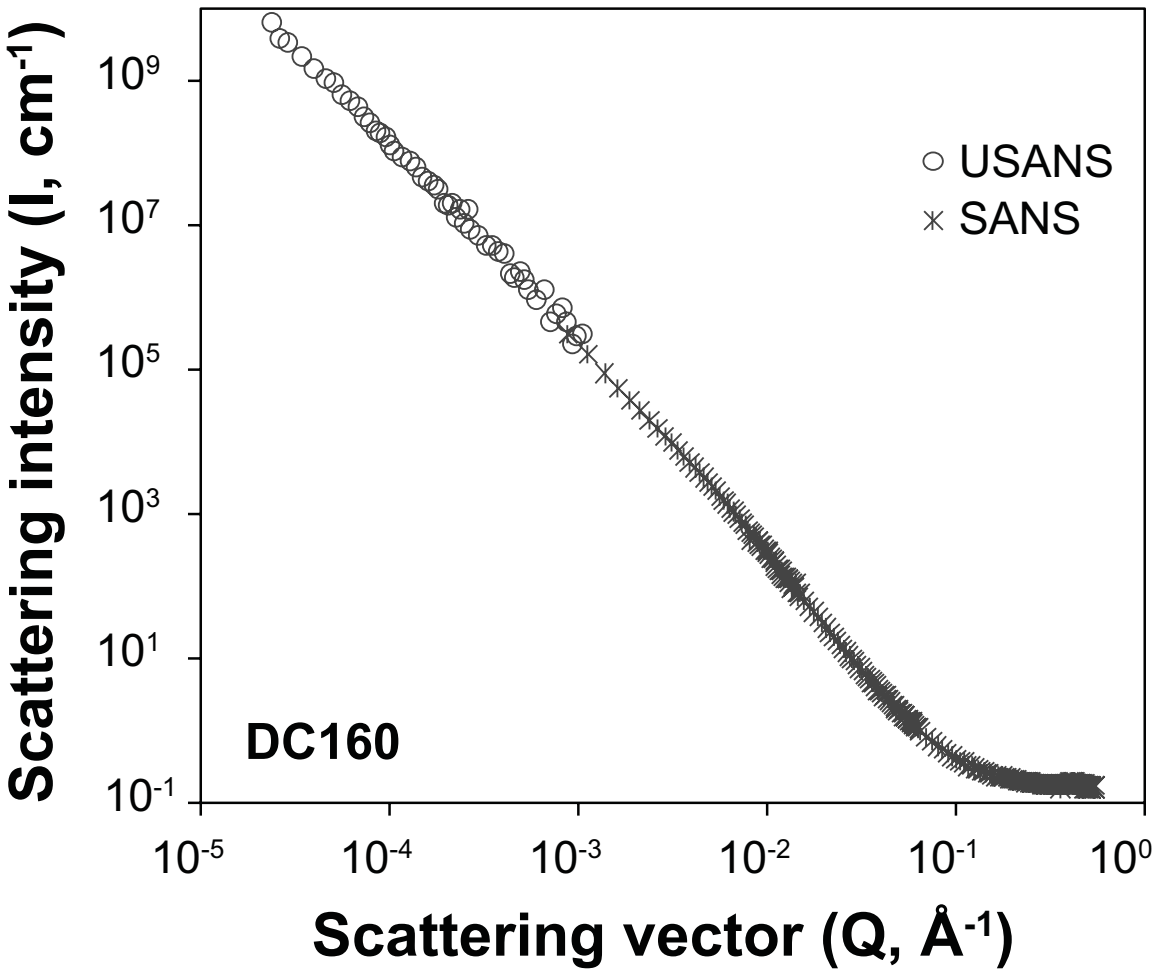
Scattering intensity (I, cm-1)
10^9
10^7
10^5
10^3
10^1
10^-1
USANS
SANS
DC160
10^-5
10^-4
10^-3
10^-2
10^-1
10^0
Scattering vector (Q, Å-1)

Figure 2.

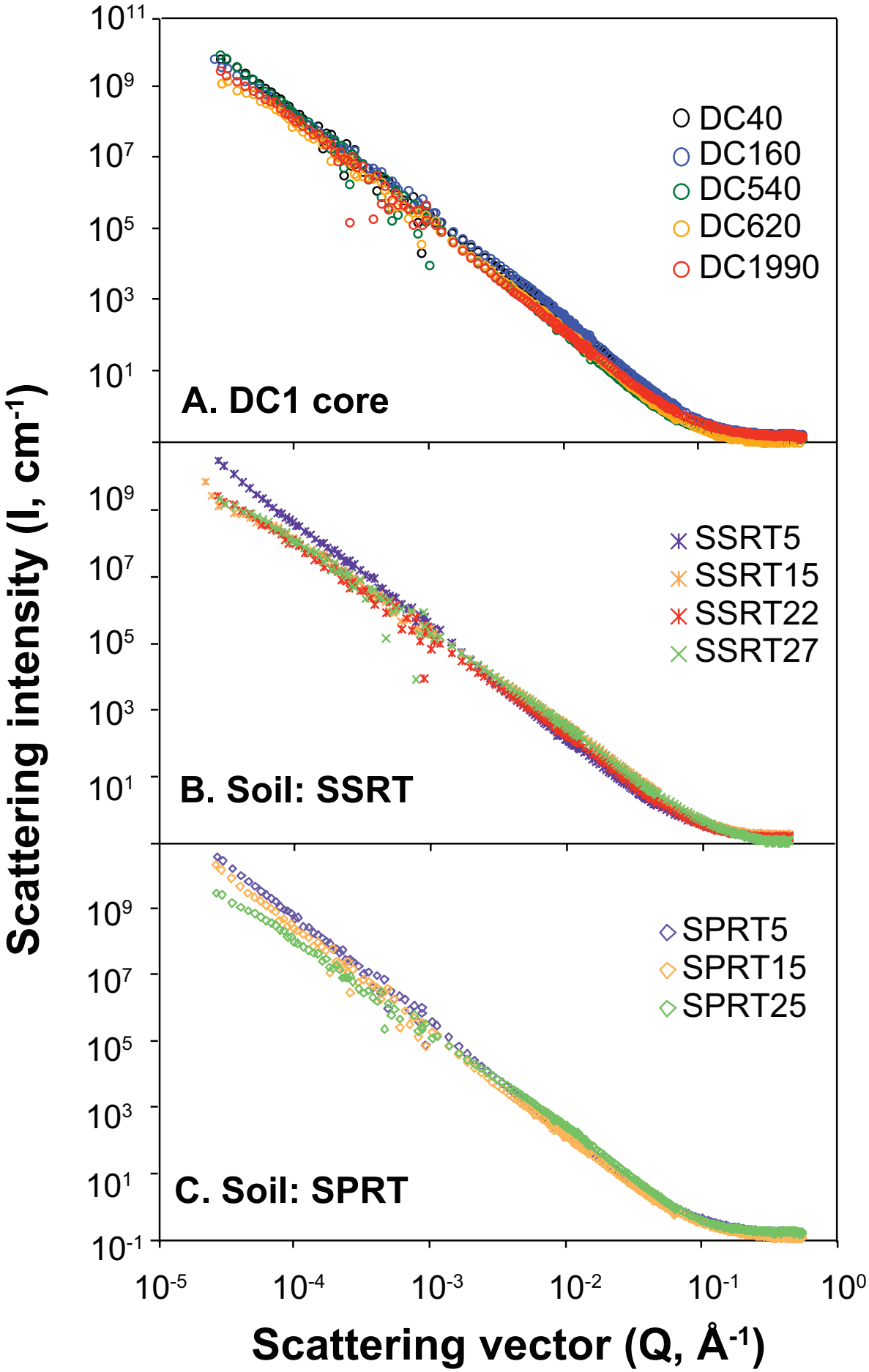
Scattering intensity (I, cm-1)
A. DC1 core
DC40
DC160
DC540
DC620
DC1990
B. Soil: SSRT
SSRT5
SSRT15
SSRT22
SSRT27
C. Soil: SPRT
SPRT5
SPRT15
SPRT25
Scattering vector (Q, Å-1)

Figure 3.

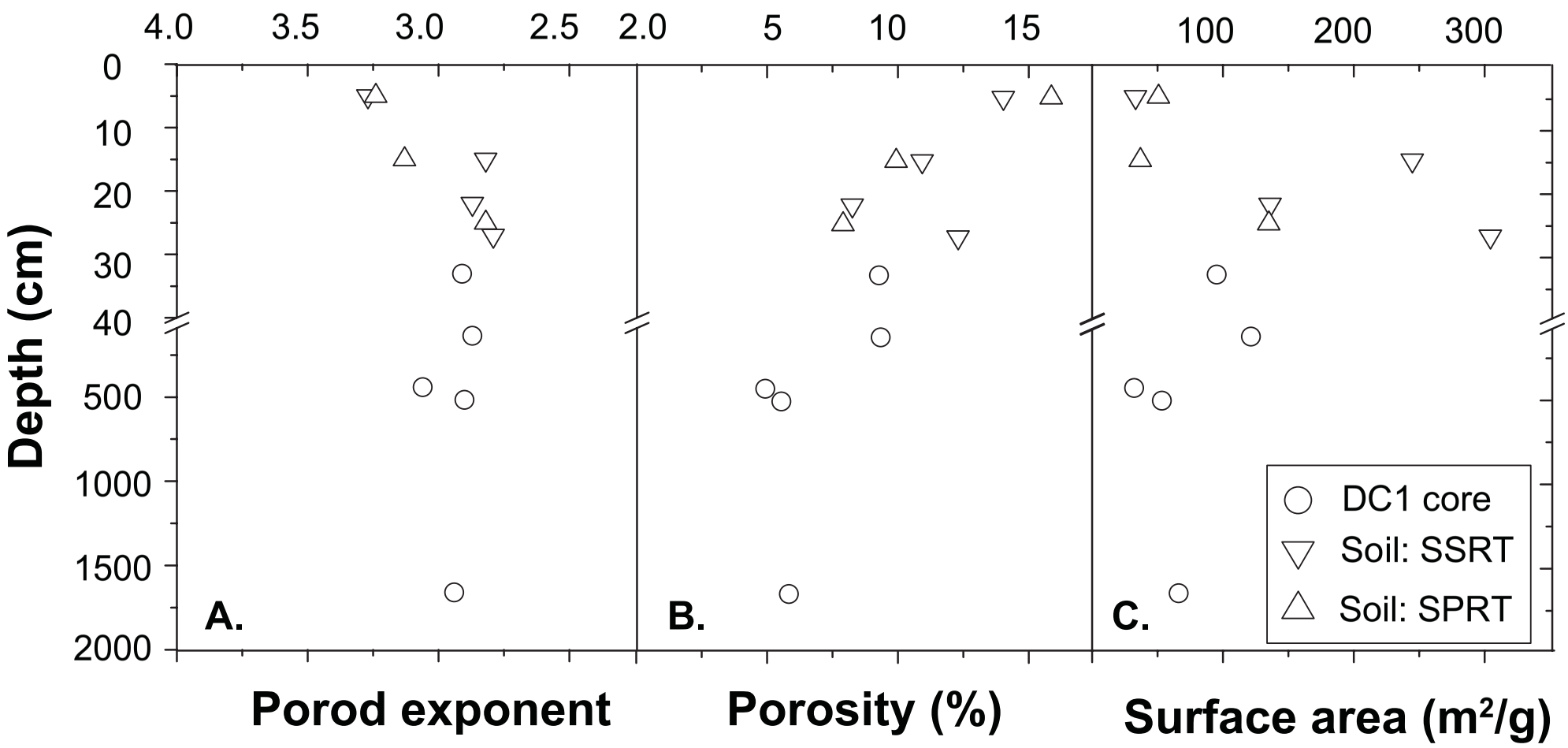
4.0
3.5
3.0
2.5
2.0
5
10
15
100
200
300
0
10
20
30
40
500
1000
1500
2000
Depth (cm)
A.
B.
C.
DC1 core
Soil: SSRT
Soil: SPRT
Porod exponent
Porosity (%)
Surface area (m²/g)

Figure 4.

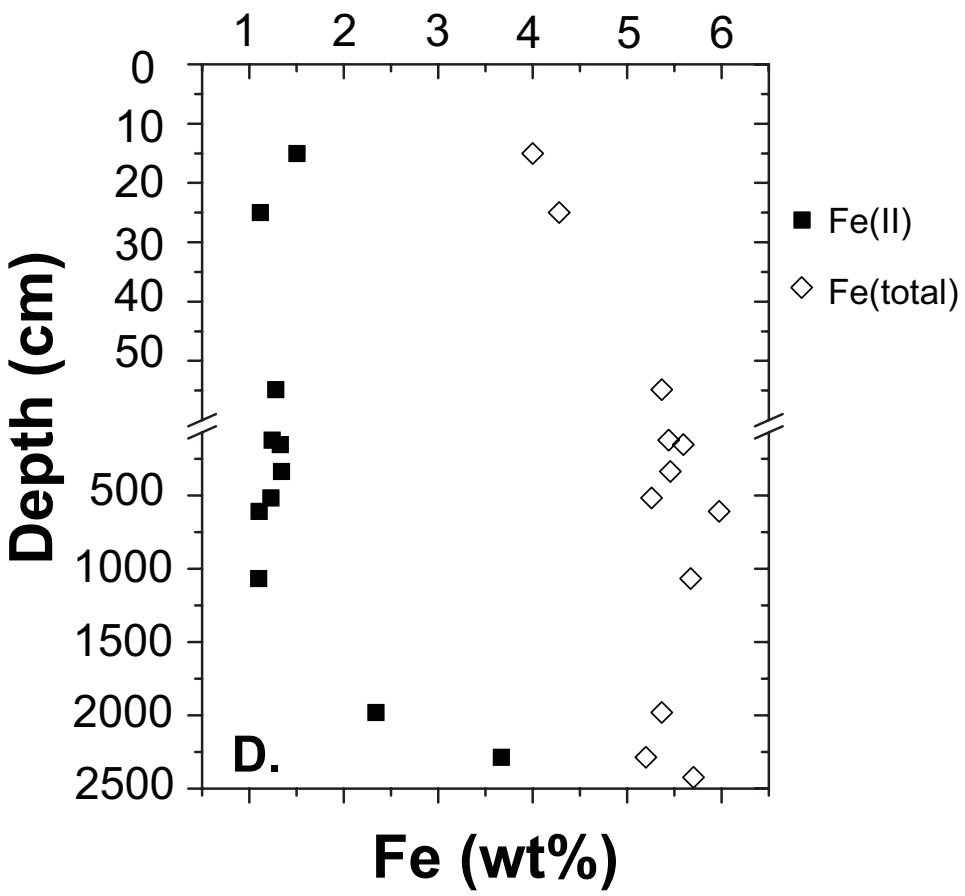
1
2
3
4
5
6
0
10
20
30
40
50
500
1000
1500
2000
2500
Depth (cm)
Fe (wt%)
D.
Fe(II)
Fe(total)

Figure 4.

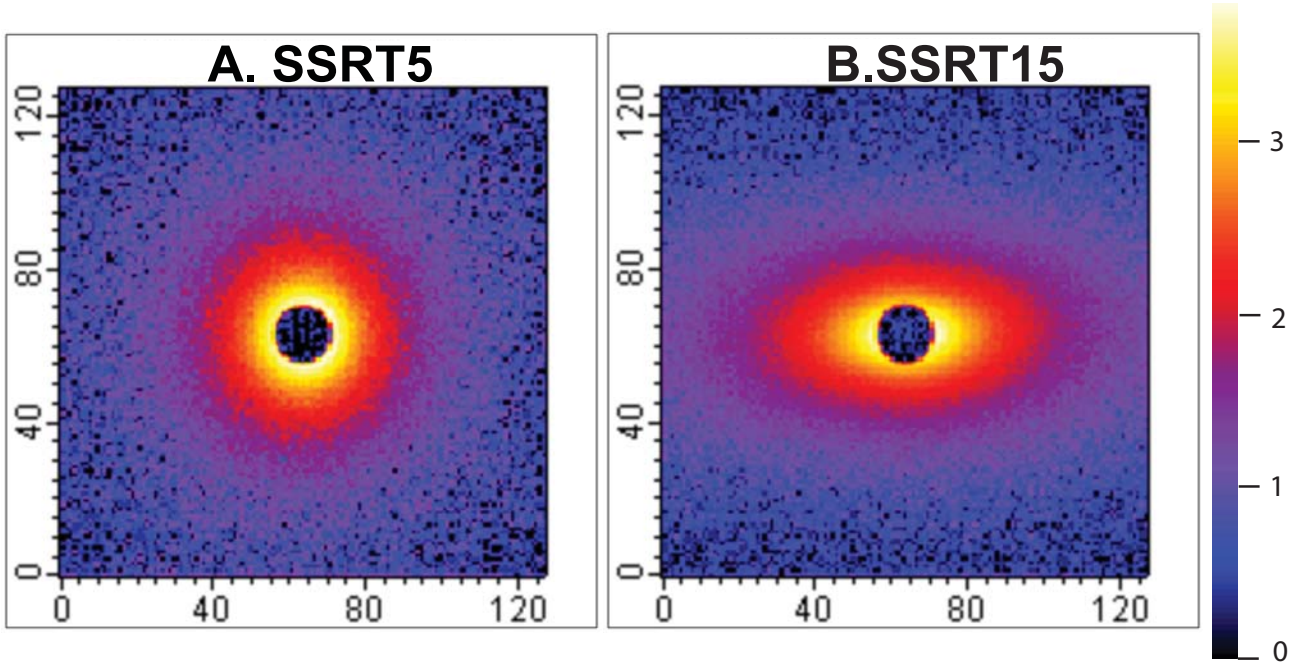

Figure 5.

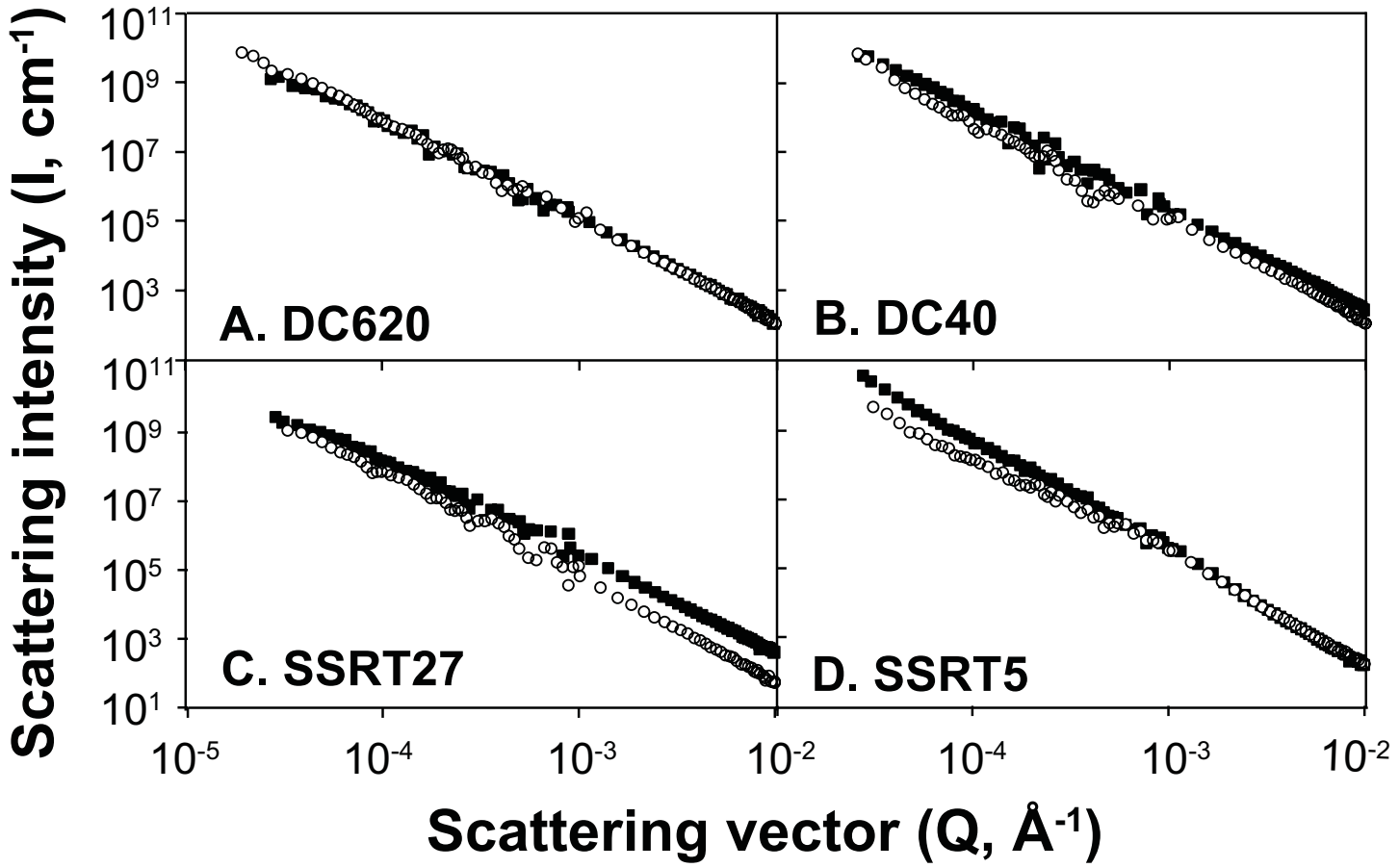
Scattering intensity (I, cm-1)
A. DC620
B. DC40
C. SSRT27
D. SSRT5
Scattering vector (Q, Å-1)

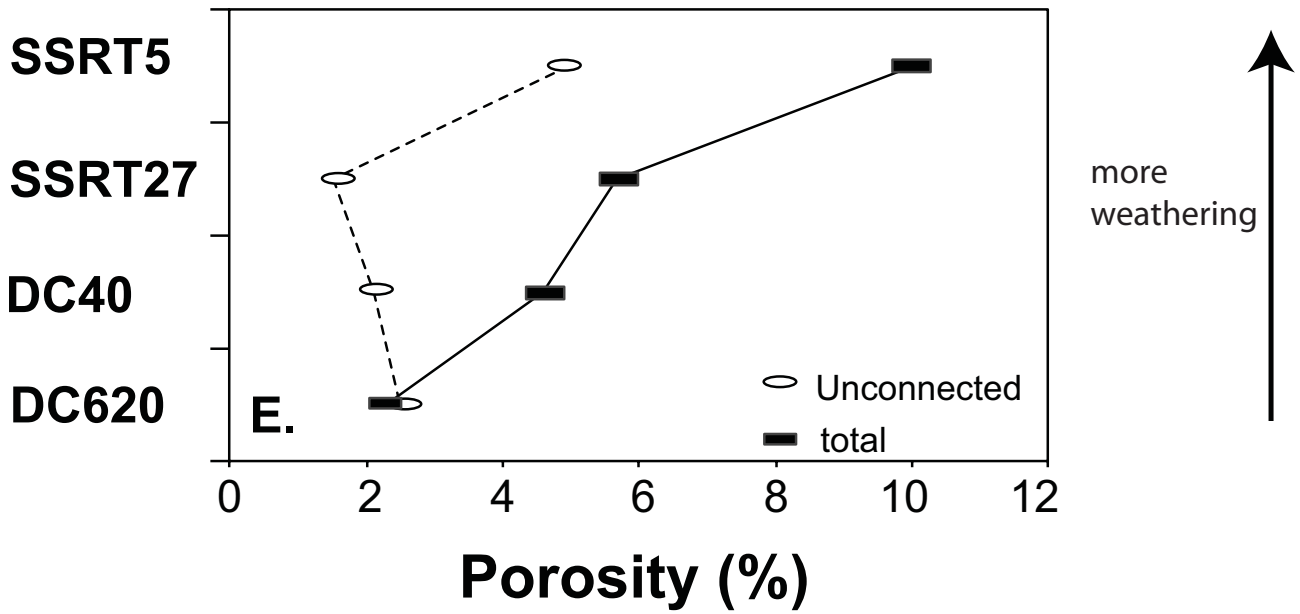
SSRT5
SSRT27
DC40
DC620
E.
Unconnected
total
more weathering
Porosity (%)

Figure 6.

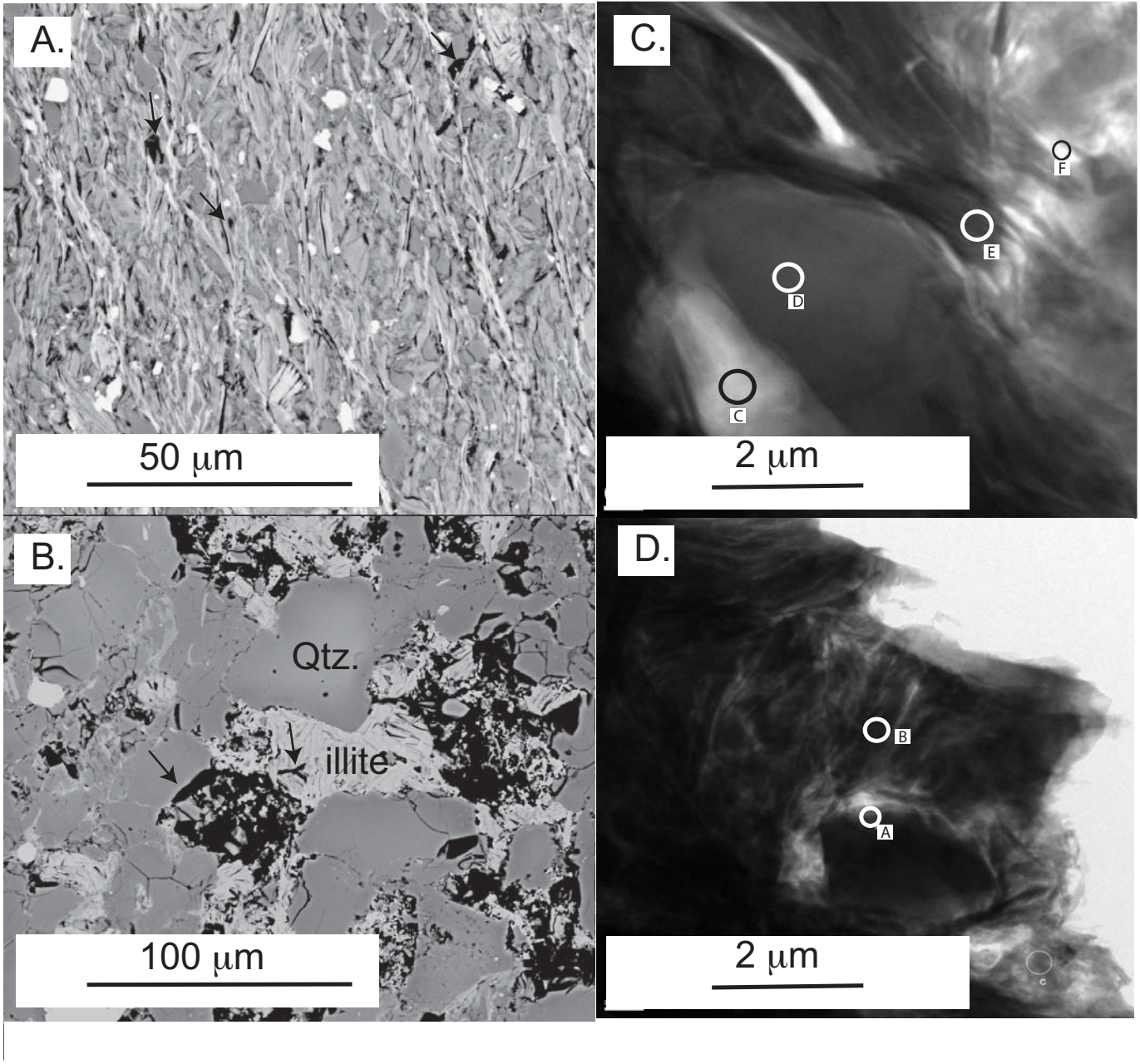

Figure 7.

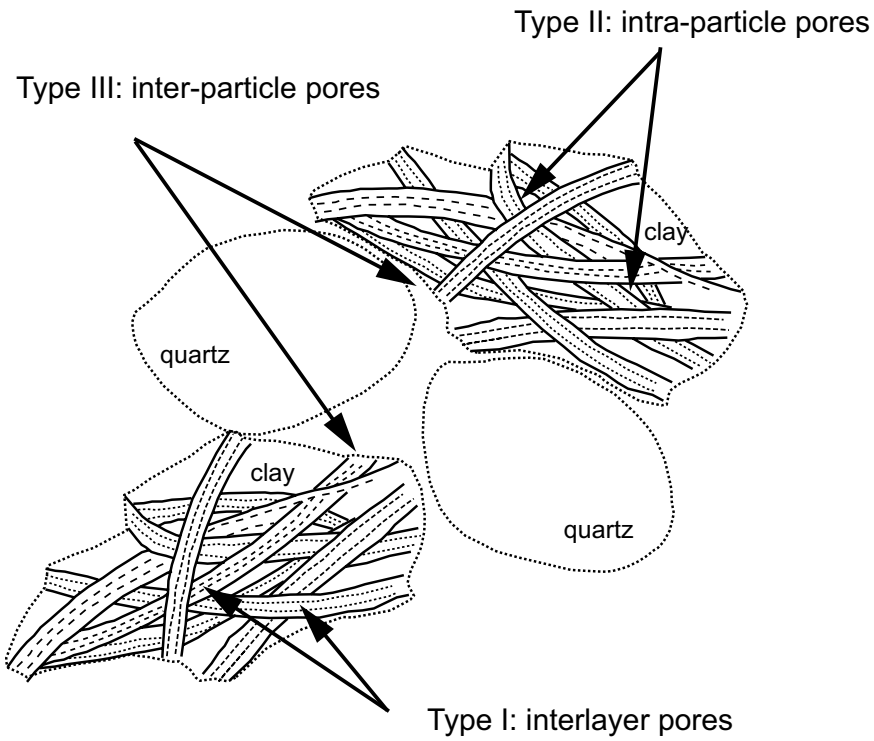
Type II: intra-particle pores
Type III: inter-particle pores
clay
quartz
clay
quartz
Type I: interlayer pores

Figure 8.

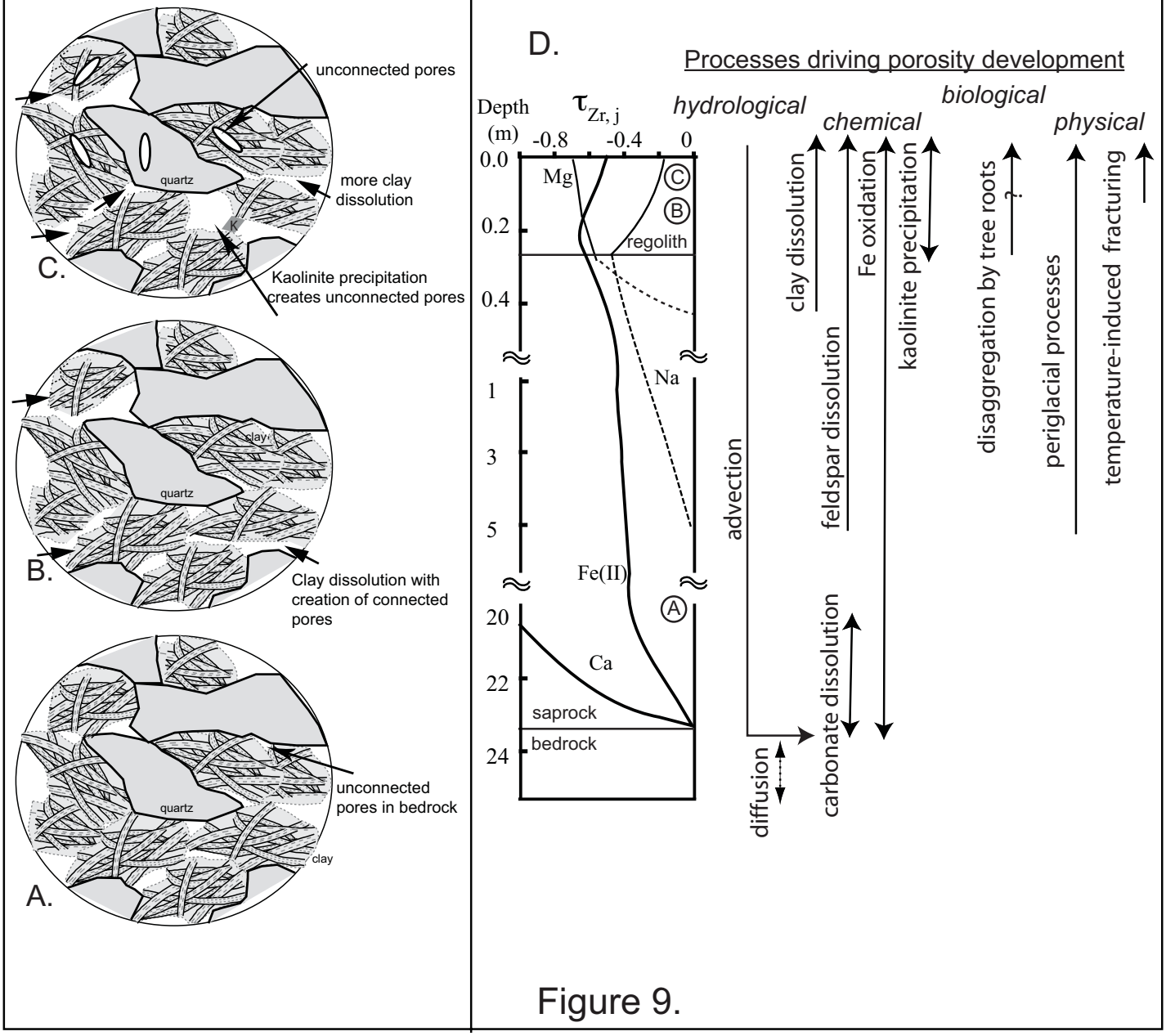
C.
unconnected pores
quartz
more clay dissolution
Kaolinite precipitation creates unconnected pores
B.
clay
quartz
Clay dissolution with creation of connected pores
A.
quartz
clay
unconnected pores in bedrock
D.
Processes driving porosity development
Depth (m)
$\tau_{Zr, j}$
-0.8
-0.4
0
0.0
0.2
0.4
1
3
5
20
22
24
Mg
Na
Fe(II)
Ca
regolith
saprock
bedrock
Ⓒ
Ⓑ
Ⓐ
hydrological
advection
diffusion
chemical
clay dissolution
feldspar dissolution
carbonate dissolution
Fe oxidation
kaolinite precipitation
biological
disaggregation by tree roots
?
physical
periglacial processes
temperature-induced fracturing

Figure 9.

Table 1: Observations and results from neutron scattering experiments

Sample number	Depth (cm)	Porod exponent[a] (n)	fractal[b] dimension	SLD[c] ($Å^{-2}$) $*10^{-6}$	Porosity (%)	Modeled exponent (n)	Modeled porosity (%)	SSA[d] (m^2/g)
Drill core samples								
DC40	30-50	2.91	2.91	3.70	9.3	2.95	6.8	95
DC160	150-170	2.87	2.87	3.72	9.3	2.92	7.6	121
DC540	520-540	3.06	2.94[b]	3.75	4.9	3.06	4.0	32
DC620	610-630	2.90	2.90	3.72	5.6	2.94	3.5	53
DC1990	1980-2000	2.94	2.94	3.74	5.8	2.91	3.8	66
Soil profile 1: SSRT								
SSRT5	0-10	3.27	2.73[b]	3.70	14.0	3.23	12.2	33
SSRT15	10-20	2.82	2.82	3.72	10.9	2.82	9.9	245
SSRT22	20-25	2.87	2.87	3.72	8.3	2.86	6.3	136
SSRT27	25-29	2.79	2.79	3.70	12.3	2.79	11.0	304
Soil profile 2: SPRT								
SPRT5	0-10	3.24	2.76[b]	3.69	15.9	3.18	12.6	51
SPRT15	10-20	3.13	2.87[b]	3.71	9.9	3.16	9.0	37
SPRT25	20-30	2.82	2.82	3.70	7.9	2.87	6.2	135

[a] Uncertainty estimated for the porod exponent is ± 0.04.

[b] samples show surface fractal, and the others exhibit mass fractal.

[c] SLD= scattering length density; [d] SSA=specific surface area.

Table 2: Total and unconnected porosity observed at $0.00003 < Q < 0.01$ $Å^{-1}$*

Sample number	Total porosity (%)	Unconnected porosity (%)	Connected porosity (%)
DC620	2.4	2.4	0.0
DC40	4.6	2.1	2.5
SSRT5	5.6	1.5	4.1
SSRT27	10.0	5.0	5.0

* Smaller range due to higher background at higher Q.

Table 3: Total and ferrous iron in soils and DC rocks

Sample number	total Fe (wt %)	ferrous Fe (wt%)
SPRT15	4.00	1.51
SPRT25	4.28	1.12
DC55	5.36	1.28
DC120	5.44	1.24
DC160	5.60	1.33
DC340	5.46	1.34
DC540	5.26	1.23
DC620	5.97	1.10
DC1066	5.67	1.10
DC1990	5.36	2.34
DC2290	5.20	3.67
DC2450	5.85	n.a.

n.a. = not available